Geoscience Frontiers 17 (2026) 102396

Contents lists available at ScienceDirect

Geoscience Frontiers

journal homepage: www.elsevier.com/locate/gsf

Research Paper

Crustal and lithospheric mantle thinning variations beneath the East African Rift System

Rasheed Ajala[a,*], Folarin Kolawole[a,b], Jean-Joel Legre[c], Tolulope Olugboji[c], Dirk-Philip van Herwaarden[d], Andreas Fichtner[d]

[a] Lamont-Doherty Earth Observatory, Columbia University, Palisades 10964, USA
[b] Department of Earth and Environmental Sciences, Columbia University, New York 10027, USA
[c] Department of Earth and Environmental Sciences, University of Rochester, Rochester 14627, USA
[d] Department of Earth and Planetary Sciences, Institute of Geophysics, ETH Zürich, Zürich 8092, Switzerland

ARTICLE INFO

Article history:
Received 23 April 2025
Revised 19 April 2026
Accepted 23 June 2026
Available online 25 June 2026

Keywords:
East African Rift System
Decoupled extension
Magma-poor rifting
Lithospheric foundering
Lithospheric delamination
Mid-lithospheric discontinuities

ABSTRACT

Knowledge gaps remain regarding strain localization mechanisms that may initiate the transition to late-phase rifting and break-up along active rifts hosted in thick continental lithosphere. Here, we conduct a multiscale study of the East African Rift System (EARS) using one of the highest-resolution seismic tomography models of Africa, along with a comprehensive compilation of lithospheric structure models from active- and passive-source seismic studies. We estimate mantle temperatures and the lithosphere-asthenosphere boundary using this model. Combined with estimated crustal thicknesses, we estimate the thinning factors of the crust and lithospheric mantle, as well as the deformation decoupling parameter, defined as the ratio of the lithospheric mantle to the crustal thinning factors. Our results reveal intriguing magnitudes of lithospheric mantle necking beneath both the eastern (magma-rich) and western (magma-poor) branches. However, the eastern branch ubiquitously exhibits commensurate crustal and lithospheric mantle thinning, whereas the western branch exhibits a complex mix of segments with coupled-thinning and those with significantly decoupled thinning. We note the key influence of inheritance, lithospheric foundering and delamination, and melt-induced ductile strain on decoupling of lithospheric thinning. The dearth of necked crust and the common occurrence of necked lithospheric mantle along the EARS suggest that necking of the lithospheric mantle probably precedes crustal necking along evolving rifts, which, where observed, manifest a weakened lithosphere primed to progressively transition to the later phases of continental extension.

1. Introduction

Continental rifting represents an integral component of Earth's evolution and the plate tectonic cycle involving the breakup of continental masses along divergent plate boundaries and the formation of oceanic basins (Wilson, 1966). Although continents host a rich record of rifting events that succeeded and those that failed to attain breakup, the currently active continental rifts exhibit variable opening rates and maturation (Kreemer et al., 2014), and it is less understood if or how the current magnitude of plate deformation manifests a tendency to attain late-stage rifting, break-up, or rift failure. The phases of rift evolution include an initial nucleation phase of the rift zone, which transitions to the stretching phase when the border faults localize, followed by the necking phase when the lithosphere thins by more than half, and then either hyperextension or oceanization before continental rupture (Fletcher and Hallet, 1983; Sutra et al., 2013; Chenin et al., 2018, 2021; Brune et al., 2023; Grant et al., 2024). However, of all these rifting phases, the necking phase is considered one of the most critical, as it represents a phase when a stretching layer is significantly thinned enough that it has lost most of its mechanical strength, giving way to strain localization and transition to late-phase extension and rupture (Fletcher and Hallet, 1983). In the lithosphere, the necking phase is accompanied by a significantly elevated thermal gradient, leading the rift to enter a regime of unstable extension (Fletcher and Hallet, 1983).

Most studies on the necking phase of rift evolution explored crustal necking and are focused on passive rifted margins or

* Corresponding author.

E-mail addresses: rajala@ldeo.columbia.edu (R. Ajala), fola@ldeo.columbia.edu (F. Kolawole), jlegre@ur.rochester.edu (J.-J. Legre), tolugboj@ur.rochester.edu (T. Olugboji), dirkphilip@gmail.com (D.-P. Herwaarden), andreas.fichtner@ erdw.ethz.ch (A. Fichtner).

https://doi.org/10.1016/j.gsf.2026.102396

exhumed fossil rifted margins (Sutra et al., 2013; Chenin et al., 2018, 2021; Chenin and Manatschal, 2025), such that little is known of how the lithospheric mantle necks and of the attendant crust-versus-mantle thinning styles from actively evolving rifts. Similarly, the driving mechanisms that promote transitions from early-stage continental rifting to late-stage remain poorly explored and need to be better understood. The two primary traditional end-member models for continental extension are active (volcanic, magma-rich) rifting and passive (nonvolcanic, magma-poor) rifting. In active rifting, the impingement of a thermal plume or anomaly rising from the asthenosphere to the base of the lithosphere provides the heat needed to thermally weaken the lithosphere, causing it to thin and generate melt. Consequently, widespread volcanism occurs. Nonvolcanic rifting involves the gradual ductile extension of the lithosphere and lower crust due to tensional forces, resulting in passive asthenospheric upwelling that further promotes rifting (Allen and Allen, 2005). The far-field plate tectonic stresses, which are on the order of ~5 TN/m (Buck, 2004), are the most significant driver among the numerous tectonic forces that cause continents to split (Brune et al., 2023). Yet the magnitude of these forces is marginal compared to the strength of a stable lithospheric column (Buck, 2004; Ajala et al., 2024). Thus, only the active rifting model, in which the heat supply drastically reduces the lithosphere's strength enough for tectonic forces to play their roles, seems intuitive and straightforward. We note, however, that the classification of continental extension models has been refined over the years, based on the increasing volume of geophysical data, to a continuum that depends on magmatic intensity and lithospheric strength and evolves through space and time (e.g., Sapin et al., 2021).

Studies of mechanisms for thinning of the lithosphere during the stretching phase of magma-poor rifts argue for the control of depth-dependent extension in which mid-crustal detachment faults decouple the upper crust from the lower crust while the lithospheric mantle is only mildly thinned (Lavier and Manatschal, 2006), or via concurrent brittle shear thinning of the upper crust and high-strength uppermost mantle assisted by mid-crustal ductile shear zones and ductile upper mantle shear zones (Brun and Beslier, 1996). However, crustal and lithospheric observations along active narrow continental rifts, such as the East African Rift System, do not support the presence of mid-crustal detachment faults (Njinju et al., 2019; Hopper et al., 2020; Brune et al., 2023). Similarly, lithospheric thickness estimates across the Malawi Rift, a tectonically active magma-poor rift still undergoing the stretching phase, show significant shallowing of the lithosphere-asthenosphere boundary (Njinju et al., 2019; Hopper et al., 2020; Brune et al., 2023), thus highlighting substantial gaps in the understanding of crustal and lithospheric thinning styles during the early phases (stretching and thinning) of rifting. Several reasons exist for the persistent knowledge gaps on continental rifting. Apart from the most obvious factor being the need for high-resolution geophysical data or models at varying spatial scales, there is a lack of incorporation or synthesis of these multiscale data and models into comprehensive studies. Numerical modeling research on continental rifting often overlooks available geophysical information in its setups or interpretation due to the simplicity of the models (Buck et al., 1988; Brune et al., 2014; Naliboff et al., 2017). Other tectonic investigations of continental rifting tend to focus on deformation at either the crustal or lithospheric scale, but not both, at a given time (Hodgson et al., 2017; Lavayssière et al., 2019; Ogden et al., 2023). Thus, the connection between the crust's feedback mechanism and the lithospheric mantle, as well as the interactive processes during continental rifting, is currently missing from the literature.

Here, we provide new insights into the mechanism behind the early phases of rifting by studying the East African Rift System (EARS) (Fig. 1). The EARS represents the ideal natural laboratory for the current undertaking because it includes examples of the two rifting endmember models — the magma-poor western branch and the magma-rich eastern branch (Fig. 1a) — with varying degrees of maturity. Furthermore, until the last decade, the eastern branch had been more instrumented than the western branch, and thus had higher-resolution geophysical models and was better studied. We study continental rifting at the crustal and mantle scales by compiling lithospheric structure models from previous seismic studies in the region and analyzing them with models of the mantle temperature and lithosphere-asthenosphere boundary (LAB) derived from one of the most up-to-date and highest resolution regional seismic tomography models of the African Plate (van Herwaarden et al., 2023). We estimate the crustal and lithospheric mantle thinning factors along the western and eastern branches of EARS, as well as the deformation decoupling factor, defined as the ratio of the lithospheric mantle to crustal thinning factors. We also compute lithospheric strength along both branches and compare it with estimates of the available far-field tectonic forces (~5 TN/m) for rifting. The new results reveal significant lithospheric mantle loss relative to crustal thinning beneath segments of the EARS, thus exposing underexplored mechanisms in continental rifting.

2. Tectonic background

The Cenozoic EARS is the largest active continental rift system on Earth and comprises two main branches – the western magma-poor branch and the eastern magma-rich branch (Fig. 1a) (Rosendahl, 1987; Ebinger, 1989; Ebinger and Sleep, 1998; Chorowicz, 2005; Ebinger, 2005; Furman, 2007; Corti, 2009, 2012). The eastern branch extends from the Afar Rift and depression in the north to the North Tanzanian Divergence Rift Zone in the south and is characterized by widespread volcanism. The western branch comprises the Albertine Rift to the north and extends south into the Coastal Plain Rift Zone, generally lacking volcanism outside a few volcanic centers, including the Rungwe Volcanic Province (RVP) just north of the Malawi Rift and Kivu, Virunga, and Toro Ankole, located between the Tanganyika and Albertine rifts. Other branches include the increasingly recognized southwestern branch extending from the northern Malawi Rift (Fig. 1a). Tomographic models and numerical studies indicate that the upwelling African Superplume may have been deflected eastward by the deeply rooted Tanzania cratonic keel, leaving the western branch magma-starved (Ebinger and Sleep, 1998; Koptev et al., 2015). Thus, based on the relative amounts of volcanism and, hence, magma input, the western branch has primarily been categorized as passive rifting, while the eastern branch can be adequately described by the active rifting paradigm.

Preexisting lithospheric weaknesses in the African Plate play a significant role in determining the location of the rift basins, such that the different rift segments in the EARS develop within the mobile belts surrounding the cratonic blocks (Rosendahl, 1987; Ebinger, 1989; Birt et al., 1997; Morley, 1999; Corti, 2009, 2012; Katumwehe et al., 2015; Kolawole et al., 2021a). These rift segments are also actively developing laterally toward a more continuous rift system (Kolawole and Ajala, 2024). The overall high elevation in the EARS (Fig. 1) is partly due to dynamic topography induced by vertical stresses in the lithosphere from the upwelling African Superplume (Nyblade and Robinson, 1994; Ebinger and Sleep, 1998; Lithgow-Bertelloni and Silver, 1998; Stamps et al., 2010; Nyblade, 2011). Except for the Turkana Depression, the eastern branch has some of the highest elevations in the region, exceeding 3 km (Fig. 1). Comparable elevations can also be found in the western branch, but these regions are mostly restricted to the localized volcanic centers and have been hypothesized to be

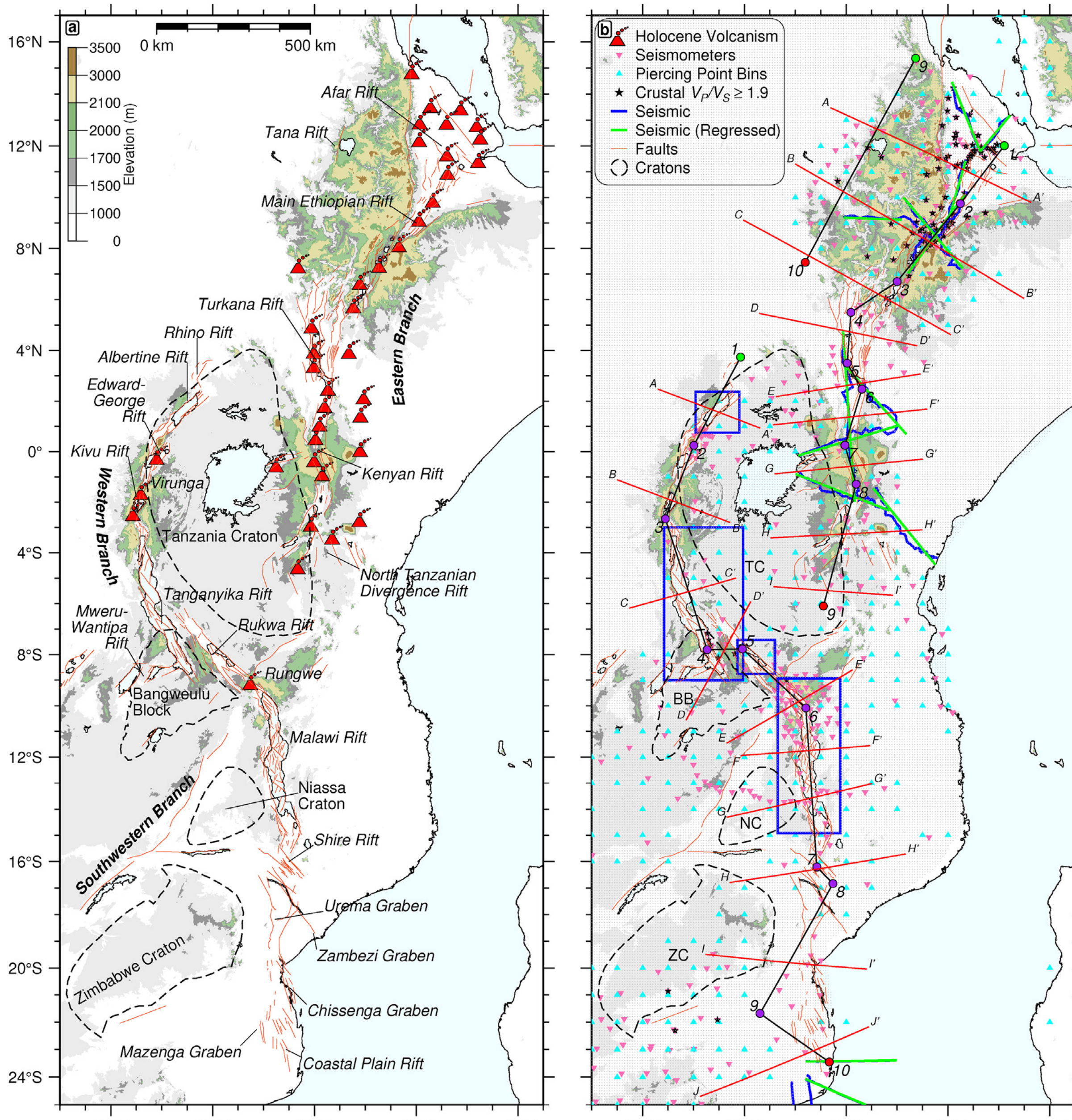

Fig. 1. Maps of the study region in the East African Rift System (EARS) and location of the utilized lithospheric structure models. (a) Relief map showing the major rift segments in the western and eastern branches of the EARS. Volcanic centers (red triangles; NCEI, 2022) emphasize the difference in surface volcanism between the two branches. Dashed black lines indicate the approximate extent of cratonic blocks, which vary considerably in the literature (Fritz et al., 2013; Koptev et al., 2015; Muirhead et al., 2020; Afonso et al., 2022). Brown lines are surficial faults (Styron and Pagani, 2020). (b) Locations of seismic stations (pink triangles) deployed in the EARS from which we compile lithospheric structure models (Last et al., 1997; Prodehl et al., 1997a, b; Dugda et al., 2005; Dugda and Nyblade, 2006; Stuart et al., 2006; Wolbern et al., 2010; Hammond et al., 2011; Reed et al., 2014; Kachingwe et al., 2015; Hodgson et al., 2017; Borrego et al., 2018; Kibret et al., 2019; Ogden et al., 2019, 2023; Sun et al., 2021; Wang et al., 2021; Petruska and Eilon, 2022; Legre and Olugboji, 2024; Sabattier and Nyblade, 2025). Blue triangles represent binned piercing points at a depth of 100 km, as determined from the receiver function study of Liu et al. (2020). Red stars indicate station locations for which crustal-averaged primary (V_P)-to-secondary (V_S) wave speed ratios (V_P/V_S) equal to or exceed 1.9, indicating crustal modification by magmatism. Blue lines and their regression (green lines) are active seismic profiles (Makris and Ginzburg, 1987; Braile et al., 1994; Gajewski et al., 1994; Maguire et al., 1994, 2006; Mechie et al., 1994, 1997; Prodehl et al., 1994, 1997b; Birt et al., 1997; Novak et al., 1997; Thybo et al., 2000; Mackenzie et al., 2005; Moulin et al., 2020, 2023; Evain et al., 2021; Lepretre et al., 2021; Watremez et al., 2021; Schnurle et al., 2023) from which we digitize crustal boundaries (i.e., basement/sediment-crust interface and Moho). Blue boxes highlight rift segments (Albertine, Tanganyika, Rukwa, and Malawi) along the western branch where we digitize sediment thickness maps primarily derived from active seismic studies (Simon et al., 2017; Kolawole et al., 2018; Muirhead et al., 2019; Scholz et al., 2020; Wright et al., 2020; Ji et al., 2023; Shaban et al., 2023; Mulaya et al., 2025; Twinomujuni et al., 2025). Small gray dots represent the grid of Moho depths from AFROMOHO (Baranov et al., 2023). The black lines with numbered checkpoints (colored circles) are the locations of the profiles along the axis of the western and eastern branches of the EARS that we analyze. Red lines are across-rift profile locations. Full name of abbreviations: BB, Bangweulu Block; NC, Niassa Craton; TC, Tanzania Craton; ZC, Zimbabwe Craton. All the compilations are provided in Ajala et al. (2026a) and shown in Fig. 2 and Supplementary Data Figs. S1–S12.

supported by additional mechanisms, such as thermal isostasy and lower-crustal dedensification (Ajala et al., 2024). The tectonic history of the rift system is complex, with some rift segments having undergone multiple phases of extension since the late Paleozoic (Ebinger, 1989, 2005; Macgregor, 2015; Kolawole et al., 2021b; Michon et al., 2022).

3. Previous seismic studies

3.1. Lithospheric structure

Several temporary and permanent seismic arrays have been deployed around the EARS (Fig. 1b) (e.g., Dugda et al., 2005; Gao et al., 2013; Reed et al., 2014; Shillington et al., 2016; Hodgson et al., 2017; Ogden et al., 2023). Several controlled-source experiments have also been conducted in the region (e.g., Prodehl et al., 1994; Maguire et al., 2006; Watremez et al., 2021). We use compilations of results on lithospheric layering beneath the East African Rift System from these studies (Figs. 1 and 2, and Supplementary Data Figs. S1 – S12).

Many seismic analyses carried out using datasets from EARS deployments have employed passive sources (e.g., earthquakes and ambient noise) and the receiver function technique (Langston, 1979). The Ps receiver function technique processes the seismic record into a time series of P-to-S wave conversions at boundaries with significant impedance contrasts, which is then used to map bulk crustal properties such as the crustal thickness (or Moho depth) and the crustal-averaged wave speed ratios (V_P/V_S). The V_P/V_S is useful for inferring crustal lithology. In general, values less than 1.80 indicate a felsic composition. Values between 1.80 and 1.90 indicate a mafic lithology, and values exceeding 1.9 suggest crustal modification by magmatism (Hammond et al., 2011; Hodgson et al., 2017). Regions with thick crust and high V_P/V_S ratios likely have underplating, while regions with thin crust and high V_P/V_S likely have partial crustal melts and fluids. On the other hand, the Sp receiver functions map S-to-P wave conversions. It helps map discontinuities in the lithospheric mantle, such as negative velocity gradients (NVGs), which serve as proxies for the lithosphere-asthenosphere boundary (LAB) and mid-lithospheric discontinuities (MLDs). The NVG is defined as the strongest negative phase in the receiver function, corresponding to a velocity decrease with depth that immediately follows the positive Moho phase. Thus, the NVG is usually interpreted as the LAB or an MLD. The crustal thickness of the eastern branch, as inferred from these passive-source studies, ranges from ~15 km in the Afar Rift to ~47 km at the North Tanzanian Divergence Rift. Crustal-averaged V_P/V_S ratios vary widely, ranging from ~1.67 to ~2.35, with the highest values observed at the Main Ethiopian Rift and Afar, where they consistently exceed 1.9. The structure at the eastern branch is generally consistent with a thinned crust resulting from rifting modified by mafic intrusion, partial melting, and fluid flow. Crustal thicknesses along the western branch vary from ~21 km at the northern end around Virunga and the Rwenzori mountains to ~51 km south of the Malawi Rift. Crustal-averaged V_P/V_S ratios range from 1.67 to 1.97, with an overall median close to 1.8 (Supplementary Data Figs. S1 – S3). Regions with values greater than 1.9 have been identified near the Rungwe Volcanic Province, north of the Malawi Rift, and at the southern Tanganyika and Rukwa Rifts, where previous research has proposed the existence of blind magmatism (Hodgson et al., 2017; Ajala et al., 2024). Thus, compared to the eastern branch, the crust of the western branch has experienced a relatively lower magnitude of thinning. Yet, the V_P/V_S values indicate a mafic composition, suggesting thermal modification. Apart from a few studies, such as Hopper et al. (2020), most local investigations focus solely on the crust. Hopper et al. (2020) employed Ps and Sp receiver function analysis to map the Moho and NVG at the northern Malawi Rift, interpreting a significantly thinned lithospheric mantle relative to the crust.

There have been extensive active source experiments conducted throughout the EARS, particularly along the eastern branch in the Afar, Main Ethiopian, Turkana, and Kenya rifts. These experiments include KRISP (e.g., Prodehl et al., 1997a, b) and EAGLE (e.g., Maguire et al., 2006), which provide 2D wide-angle seismic reflection and refraction profiles that image the crustal structure with high resolution (Supplementary Data Figs. S4–S7). Results from the experiments have revealed magmatic underplating in the Ethiopian Rift and significantly thinned crust beneath Afar and Turkana. Along the western branch, 2D wide-angle seismic reflection and refraction experiments have also been conducted. These experiments include PAMELA (e.g., Evain et al., 2021) in the Mozambique Coastal plains and offshore and other seismic reflection surveys in the Albertine, Tanganyika, Rukwa, and Malawi rifts (e.g., Simon et al., 2017; Scholz et al., 2020; Wright et al., 2020; Mulaya et al., 2025). The density of active-source seismic profiles in these rifts has enabled high-resolution estimates of sediment thicknesses (Supplementary Data Figs. S8 and S9). Some of the active source data collected in the western branch have been used in 3D local tomography studies (e.g., Accardo et al., 2018). In general, crustal thickness estimates from active-source data are comparable to those from passive-source experiments where they overlap (e.g., Khan et al., 1999; Mackenzie et al., 2005). However, active-source experiments have lower uncertainties due to known source locations and high station coverage (e.g., Watremez et al., 2021). Compilations of active- and passive- source crustal models in the region have been synthesized to produce a Moho map for Africa (AFROMOHO; Baranov et al., 2023). We use a dataset similar to that of Baranov et al. (2023) in the current study (Figs. 1b and 2b, and Supplementary Data Fig. S11). However, our compilations include more recent lithospheric models, e.g., those of Sabattier and Nyblade (2025) for the Mozambique Coastal Plains and southeastern Tanzania, which postdate AFROMOHO and were thus not used in its development.

Several regional-to-local seismic tomography studies have been conducted to map the crust and mantle structure of the African plate (Fishwick, 2010; Adams et al., 2012; Civiero et al., 2016; Domingues et al., 2016; Accardo et al., 2018, 2020; Emry et al., 2019; Celli et al., 2020; Korostelev et al., 2022; Boyce et al., 2023; van Herwaarden et al., 2023; Kolawole and Ajala, 2024; Olugboji et al., 2024). The more local-scale models have been developed along both the western and eastern branches, including in the Tanganyika-Rukwa region (Kolawole and Ajala, 2024), Northern Malawi Rift (Accardo et al., 2018, 2020), Mozambique Coastal Plains (Domingues et al., 2016), Afar and the Main Ethiopian Rift (Gallacher et al., 2016; Chambers et al., 2022), Turkana (Kounoudis et al., 2021), and North Tanzanian Divergence (Tiberi et al., 2019). Some early regional-scale models, such as the surface wave tomography model developed by Fishwick (2010) and O'Donnell et al. (2013), may have contributed to the persistence of the knowledge gap of rifting in the western branch. These models exhibit relatively continuous, fast mantle wave speeds, like those observed in current global-scale models (e.g., Priestley et al., 2024), beneath the western branch, which supports the argument for a cold, thick lithosphere. However, newer regional models incorporate new data and are developed using full-waveform inversion, a sophisticated seismic imaging technique (Tarantola, 1984; Virieux and Operto, 2009; Tromp, 2020), resulting in higher tomographic resolution (Supplementary Data Figs. S13–S28). In particular, the model of van Herwaarden et al. (2023) shows more delimited lithospheric heterogeneities and highlights that the regions of low shear wave speeds along the western branch are not limited to the volcanic centers. The thermal LAB inferred from existing seismic tomography models shows very shallow depths (≤ 40–60 km) at the eastern branch and much deeper depths (≥ 150 km) along the western branch (Fishwick, 2010; Afonso et al., 2022; Priestley et al., 2024). The thermal LAB derived from these studies differs from the LAB determined from receiver functions: the former involves converting seismic wave speeds to temperature, whereas the latter identifies regions of decreasing wave speeds with depth (i.e., Negative Velocity Gradients (NVGs) in receiver functions). However, the NVGs cannot always be interpreted as the LAB and are sometimes a mid-lithospheric discontinuity (MLD). The "chemical" LAB can also be determined from petrological data by constructing thermobarometers (temperature–pressure paths) from mantle melt and can be jointly inverted with seismological constraints (e.g., Plank and Forsyth, 2016).

3.2. Lithospheric models utilized in this study

3.2.1. Lithospheric structural models from active and passive source studies

We use compilations of lithospheric structure models, primarily sediment thickness or basement (sediment-crust interface) depths, Moho depths, crustal-averaged V_P/V_S (whenever available from receiver function studies), and NVGs (whenever available from receiver function studies) in the region (Ajala et al., 2026a) (Fig. 2 and Supplementary Data Figs. S1–S12). Most passive-source models derived from receiver functions are provided as station-averaged results, which can be easily incorporated into our analysis (Supplementary Data Figs. S1–S3). These passive source compilations (Last et al., 1997; Prodehl et al., 1997a, b; Dugda et al., 2005; Dugda and Nyblade, 2006; Stuart et al., 2006; Wolbern et al., 2010; Hammond et al., 2011; Reed et al., 2014; Kachingwe et al., 2015; Hodgson et al., 2017; Borrego et al., 2018; Kibret et al., 2019; Ogden et al., 2019, 2023; Liu et al., 2020; Sun et al., 2021; Wang et al., 2021; Petruska and Eilon, 2022; Legre and Olugboji, 2024; Sabattier and Nyblade, 2025) are shown in Supplementary Data Figs. S1–S3. We exclude the Moho depth compilations of Liu et al. (2020) from our analysis because they are located at 100-km depth piercing-point bins, which cannot be used to determine the station location and will introduce large horizontal location errors. We, however, use NVGs from their study to interpret our results, since they are mostly located in the mantle and closer to the 100 km piercing-point bins. Most of our compilations from the passive-source studies provide only Moho depths, except for Sabattier and Nyblade (2025), which also determined sediment thicknesses in southeast Tanzania and the Mozambique Coastal Plains (Fig. 2a and Supplementary Data Fig. S10). For the active source studies that mostly include 2D wide-angle seismic reflection and refraction profiles (Makris and Ginzburg, 1987; Braile et al., 1994; Gajewski et al., 1994; Maguire et al., 1994, 2006; Mechie et al., 1994, 1997; Prodehl et al., 1994, 1997a, b; Birt et al., 1997; Novak et al., 1997; Thybo et al., 2000; Mackenzie et al., 2005; Moulin et al., 2020, 2023; Evain et al., 2021; Lepretre et al., 2021; Watremez et al., 2021; Schnurle et al., 2023), we digitize the modeled sections at 1-km grid spacing to provide estimates of sediment and crustal thicknesses (Supplementary Data Figs. S4–S7). Moho depths from the PAMELA profiles in the Mozambique Coastal Plains were excluded from our analysis because the models lacked onshore Moho ray coverage (e.g., Watremez et al., 2021). We digitize sediment thickness maps on a 0.05° by 0.05° (~5 km by 5 km) grid from active source studies along the western branch in the Albertine, Tanganyika, Rukwa, and Malawi rifts (Simon et al., 2017; Kolawole et al., 2018; Muirhead et al., 2019; Scholz et al., 2020; Wright et al., 2020; Ji et al., 2023; Shaban et al., 2023; Mulaya et al., 2025; Twinomujuni et al., 2025) (Supplementary Data Fig. S8). These sediment thickness grids were combined with estimates from the 2D seismic profiles to generate an active-source sediment

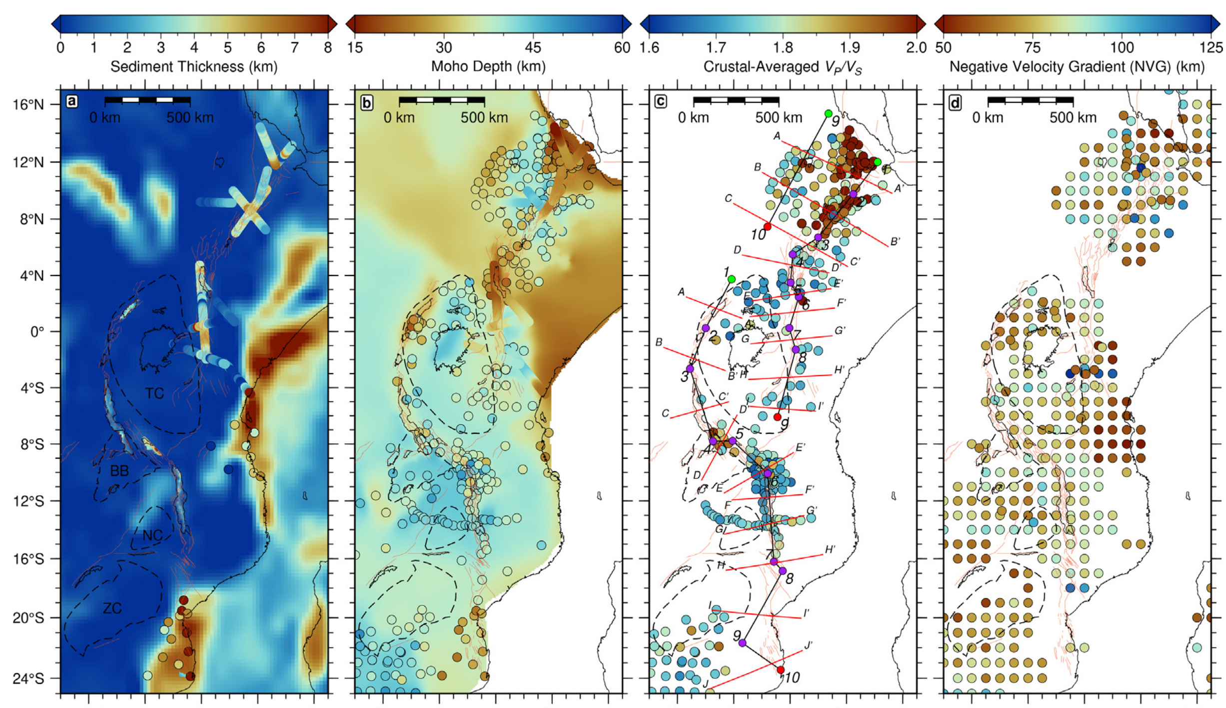

Fig. 2. Compilation of lithospheric structure models from active- and passive-source studies. (a) Sediment thickness grid from CRUST1.0 (Laske et al., 2013) and active-source-derived sediment thickness maps (i.e., detailed grid along the Albertine, Tanganyika, Rukwa, and Malawi rifts), and from active and passive source models (colored circles). (b) Moho depth grid from the African Moho model (AFROMOHO, Baranov et al., 2023) and from the compilations of active- and passive-source models (colored circles). (c) Crustal-averaged V_P/V_S ratios compiled from passive source models (i.e., receiver functions). (d) Negative Velocity Gradients (NVGs) compiled from passive source models (i.e., receiver functions). The NVG represents the strongest negative phase following the receiver function Moho and is usually interpreted as the lithosphere-asthenosphere boundary (LAB) or mid-lithospheric discontinuity (MLD). Full name of abbreviations: BB, Bangweulu Block; NC, Niassa Craton; TC, Tanzania Craton; ZC, Zimbabwe Craton. Supplementary Data Figs. S1–S12 show the compilations and uncertainties (Ajala et al., 2026a).

thickness map for the region using nearest-neighbor interpolation (Supplementary Data Fig. S9). However, because most active-source models are 2D, a grid can be generated only when the seismic profiles are closely spaced. Thus, the sediment thickness grid is sparse outside of the rift basins along the western branch (Supplementary Data Fig. S9). Sediment thickness estimates elsewhere, where the active-source models are unavailable, are determined from CRUST 1.0 (Laske et al., 2013) (Fig. 2a and Supplementary Data Fig. S10). We also utilize AFROMOHO (Baranov et al., 2023) to provide Moho depth estimates where models from our active- and passive-source compilations are unavailable (Figs. 1b and 2b, and Supplementary Data Fig. S11).

We compile uncertainties in Moho depths from passive-source (receiver function) studies when available (Supplementary Data Figs. S1–S3). For the models from Legre and Olugboji (2024), which do not provide uncertainties, we estimate the uncertainties in the Moho and NVG depths from the widths of their associated phases in the receiver function waveforms (Supplementary Data Fig. S2). For AFROMOHO (Baranov et al., 2023) and other passive-source models (Wolbern et al., 2010; Wang et al., 2021; Sabattier and Nyblade, 2025) with unreported uncertainties, we assign a standard Moho depth error of 3 km, which is the average uncertainty in the Hκ-stacking procedure used to determine crustal thickness in receiver function studies (Zhu and Kanamori, 2000; Baranov et al., 2023). The 3 km uncertainty is also the upper bound of the interpolation errors reported in AFROMOHO by Baranov et al. (2023). For active-source studies, which have higher resolution than passive-source studies owing to the certainty in source locations and the density of seismic stations, we assign a standard Moho depth error of 1 km based on resolution tests (e.g., Watremez et al., 2021).

Differences in sediment thickness estimates between CRUST1.0 and our active-source compilations at the sites of the active-source models range from −9.92 to 4.37 km, with CRUST1.0 mostly underestimating sediment thicknesses beneath the rift basins and overestimating them along the coastal plains (Fig. 2a and Supplementary Data Fig. S10). Although AFROMOHO was developed using a similar compilation of active- and passive-source data, the difference in Moho depths between AFROMOHO and our compilations ranges from −12.65 to 16.70 km (Fig. 2b and Supplementary Data Figs. S11). We attribute the difference to the kriging procedure used in Baranov et al. (2023) to generate a continuous Moho map. Along the western branch, Moho depths are shallowest at the Albertine and Mozambique Coastal Plains, and in Turkana and Afar in the eastern branch (Fig. 2b). Sediment thickness is greatest (~9 km) in the southern Rukwa rift and Mozambique Coastal Plains in the western branch, and in the Kenyan rift along the eastern branch (Fig. 2a). Supplementary Data Fig. S12 shows the compiled crustal thicknesses with and without sediments removed. Our compilations of sediment thickness, Moho depths, crustal-averaged V_P/V_S ratios, and NVGs, along with their uncertainties, are provided in Ajala et al. (2026a).

3.2.2. Anisotropic shear wave speed tomography model

Over the past decade, several regional and global-scale tomographic models have been developed with good coverage over the EARS. Among the available regional models, we focus our analysis on the full-waveform tomography result of van Herwaarden et al. (2023), which represents one of the most up-to-date and highest-resolution Earth models for the African Plate and uses waveform data with a minimum period of 35 s. Besides the high resolution in the model, we selected it owing to the availability of anisotropic shear wave speeds (V_{SV} and V_{SH}), which we require, to utilize the methodology (Priestley and McKenzie, 2006, 2013; Priestley et al., 2024) for determining the thermal lithosphere-asthenosphere boundary (LAB). We use the wave speeds of vertically polarized *S* waves (V_{SV}). We note, however, that other methods for estimating the thermal LAB exist that use isotropic wave speeds (V_S) (e.g., Goes et al., 2000). Thus, we make comparisons of the V_S in the model of van Herwaarden et al. (2023), determined using the Voigt average of V_{SH} and V_{SV}, to the V_S from other models of comparable scale, resolution, and development technique (i.e., full waveform inversion) (Emry et al., 2019; Celli et al., 2020). In general, the models exhibit similar structures (Supplementary Data Figs. S13–S21), but the model of van Herwaarden et al. (2023), shows more pronounced structural heterogeneities. The reason for the higher resolution in the model is discussed in van Herwaarden et al. (2023), namely that Emry et al. (2019) uses empirical Green's functions extracted from ambient noise rather than earthquakes, which can introduce artifacts, and Celli et al. (2020) compute model updates using misfit gradients derived with a constant 1D model rather than an evolving 3D model. We also compare the crustal parts of the model with a recently developed high-resolution regional crustal model of the African plate, derived from short-period (5–40 s) ambient noise tomography (Olugboji et al., 2024) (Supplementary Data Figs. S22–S28). Similarities in crustal structure between the two models, except for the low wave speeds beneath the rift basins captured in the model of Olugboji et al. (2024) and missing in the model of van Herwaarden et al. (2023), underscore the high resolution of the van Herwaarden et al. (2023) model since it was developed to focus on mantle structure using waveforms with periods greater than 35 s. Uncertainties in the model are generally below 50 m/s, particularly in the upper mantle, corresponding to an upper-bound error of 1% (van Herwaarden et al., 2023).

As previously noted, several other tomographic models have been developed throughout the region at a more local scale that image the upper mantle at high resolution (e.g., Adams et al., 2012; Domingues et al., 2016; Gallacher et al., 2016; Accardo et al., 2018, 2020; Tiberi et al., 2019; Kounoudis et al., 2021; Chambers et al., 2022). These models can be synthesized with existing, more regional-scale models (e.g., Emry et al., 2019; Celli et al., 2020; van Herwaarden et al., 2023) using, for example, merging techniques (Ajala and Persaud, 2021, 2022; Ajala et al., 2025) to produce high-resolution, multiscale tomographic models that provide improved constraints on the lithospheric structure in the region.

4. Methods

4.1. Converting wave speeds of vertically polarized s waves (V_{SV}) to temperature T (V_{SV})

To estimate the LAB from the tomography model of van Herwaarden et al. (2023), we follow the approach of Priestley and McKenzie (2006), noted to produce similar results as the method described by Priestley and McKenzie (2013) and Priestley et al. (2024), with the later studies involving the use of higher-resolution tomography models. The wave speeds of vertically polarized *S* waves (V_{SV}) are parameterized as a function of temperature and pressure. Then, a Newton optimization procedure determines the temperature value that minimizes the difference between the observed and predicted wave speed.

V_{SV} is given as a function of pressure P, temperature $T_{SV} \stackrel{\text{def}}{=} T(V_{SV})$ in °C, and an activation process a,

$$V_{SV} = V_{SV}(P, T_{SV}, a) \tag{1}$$

where

$$a = A' e^{\frac{-(E+PV_a)}{R(T_{SV}+273.15)}} \tag{2}$$

where $A'\left(-1.8\times10^{13}\ \mathrm{km\,s^{-1}}\right)$ is the frequency factor, $E\left(409\ \mathrm{kJ\,mol^{-1}}\right)$ is the activation energy, $V_a\left(10\times10^{-6}\ \mathrm{m^3\,mol^{-1}}\right)$ is the activation volume, and $R\left(8.314\ \mathrm{J\,K^{-1}\,mol^{-1}}\right)$ is the universal gas constant. By isolating the nonactivated component of the pressure dependence of V_{SV}, we can write

$$V_{SV}{}^{*}=\frac{V_{SV}}{1+b_V(z-50)} \tag{3}$$

where $b_V\left(3.84\times10^{-4}\ \mathrm{km^{-1}}\right)$ is an empirical constant and z is depth in km. Using a Taylor series expansion to expand $V_{SV}{}^{*}$ to first order, i.e.,

$$V_{SV}{}^{*}(a)=V_{SV}{}^{*}(0)+\left(\frac{\partial V_{SV}{}^{*}}{\partial a}\right)_0 a \tag{4}$$

gives

$$V_{SV}{}^{*}=mT_{SV}+c+a \tag{5}$$

where $m\left(-2.8\times10^{-4}\ \mathrm{km\,s^{-1}C^{-1}}\right)$ and $c(4.72\ \mathrm{km\,s^{-1}})$ are empirical constants. T_{SV} is then iteratively inverted from Eq. (5) using the Newton-Raphson method by setting the following initial value

$$T_{SVi}=\begin{cases}\frac{V_{SV}{}^{*}-c}{m}, & (V_{SV}{}^{*}>4.4\ \mathrm{km\,s^{-1}})\\ 1000\ ^{\circ}\mathrm{C}, & (V_{SV}{}^{*}\le 4.4\ \mathrm{km\,s^{-1}})\end{cases} \tag{6}$$

and minimizing

$$\chi(T_{SV})=mT_{SV}+c+a-V_{SV}{}^{*} \tag{7}$$

as follows

$$T_{SVi+1}=T_{SVi}-\frac{\chi(T_{SVi})}{\chi'(T_{SVi})} \tag{8}$$

where

$$\chi'(T_{SVi})=m+\left(\frac{E+PV_a}{R(T_{SVi}+273.15)^2}\right)a \tag{9}$$

4.2. Modeling the thermal lithosphere-asthenosphere boundary (LAB)

Due to uncertainties in the absolute temperature estimates, particularly at lower temperatures or shallower depths (Fishwick, 2010) (e.g., Supplementary Data Fig. S29), we do not determine the LAB using a simple temperature contour. Instead, at each grid point in the model space, we fit a steady-state continental geotherm parameterized as a function of the surface heat flow q_0, within the 30 to 90 mW/m^2 range, to the V_{SV}-derived temperature estimates at depths below 40 km. We then define the LAB at the 1300 °C isotherm (Ajala et al., 2024) (Fig. 3 and Supplementary Data Fig. S29). We, thus, solve

$$\underset{q_{0\in[30,90]},\ z\ge 40\ \mathrm{km}}{\arg\min}\ \|T(q_0)-T(V_{SV})\|_{l^2} \tag{10}$$

using directed grid search, with a q_0 step size of 1 mW/m^2, and for depths equal to and exceeding 40 km. The LAB is then determined as the 1300 °C isotherm in $T(q_0)$. $T(q_0)$ is derived by solving the Poisson temperature equation

$$\Delta T=-\frac{H}{k} \tag{11}$$

where H is the volumetric heat production in μWm^{-3} and k is the thermal conductivity in Wm^{-1}K^{-1}. Taking the surface heat flow q_0 and surface temperature T_0 as boundary conditions and integrating Eq. (11) twice gives

$$q_0=q_z+Hz \tag{12}$$

and

$$T_z=T_0+\frac{q_0}{k}z-\frac{H}{2k}z^2 \tag{13}$$

where q_z and T_z are heat flow and temperature at depth z, respectively. We partition the surface heat flow in the upper crust to be 40% and 60% from radiogenic and deeper mantle sources, respectively, and assume a volumetric heat production $H(z)$ that decays exponentially with depth as

$$H(z)=H_0e^{-\frac{z}{D}} \tag{14}$$

where H_0 is the surface radiogenic heat production and D (10 km) is the radiogenic length.

$$H_0=0.4\times\frac{q_0}{D} \tag{15}$$

The upper-crustal volumetric heat production decays until it matches the lower-crustal value, and the convective geotherm is calculated using a potential mantle temperature of 1300 °C and an adiabatic gradient of 0.4 K km^{-1}. The approach used to derive $T(q_0)$ is similar to that of Chapman (1986) and Ajala et al. (2024). Values for the modeling parameters are in Supplementary Data Table S1. The maximum q_0 value of 90 mW/m^2 imposes an LAB minimum of ~56.8 km in the model. Additionally, we impose a maximum LAB of 250 km. Fig. 3 shows the fits between the steady-state geotherms and the V_{SV}-derived temperature models at select locations. We do not use observed surface heat flow measurements as constraints in the optimization because we do not have estimates of crustal temperatures or variations of crustal heat production, thermal conductivities, and near-surface conditions in the region that can significantly modify the mantle-predicted heat flows (Fig. 3a and Supplementary Data Fig. S30). The geotherm is parameterized as a function of heat flow for simplicity and computational convenience, allowing a single parameter to be varied while others are held fixed (Supplementary Data Table S1). The main purpose of the steady-state geotherm is to fit mantle temperatures. Nonetheless, the mantle-predicted heat flow is generally consistent with observations (Fig. 3a and Supplementary Data Fig. S30).

To determine model uncertainties, we perturb the V_{SV} by 1%, which represents the maximum uncertainty in the wave speeds (van Herwaarden et al., 2023), and repeat the modeling procedure. Supplementary Data Fig. S29 illustrates the approach using the reference PREM model (Dziewonski and Anderson, 1981). A 1% perturbation in the PREM wave speeds results in temperature differences of up to ± 164 °C, heat flow differences of –4 to 5 mW/m^2, and LAB perturbations of –24 to 27 km (Supplementary Data Fig. S29). The estimated uncertainties are asymmetric (Supplementary Data Fig. S29) due to the nonlinearity of the modeling procedure.

We show the V_{SV}, V_{SV}-derived temperature, LAB, and the average LAB uncertainties in Fig. 4. We symmetrize the LAB uncertainties by averaging the differences between the perturbed and unperturbed LAB estimates. The uncertainties are poorly constrained at the model's extrema, corresponding to heat flow values of 30 mW/m^2 and 90 mW/m^2, where the model is either too hot or too cold. These areas are highlighted in pink in Fig. 4d. As we later discuss, while the uncertainties in these regions are not well constrained, their values are likely near zero due to other geologic and crustal model constraints, e.g., the LAB cannot be shallower than the Moho. Supplementary Data Fig. S32 compares our results with those of Priestley et al. (2024), as we use a similar approach. We, however, note that Priestley et al. (2024) develop a global-scale tomographic V_{SV} model using ray theory, and thus their model has lower resolution than that of van Herwaarden et al.

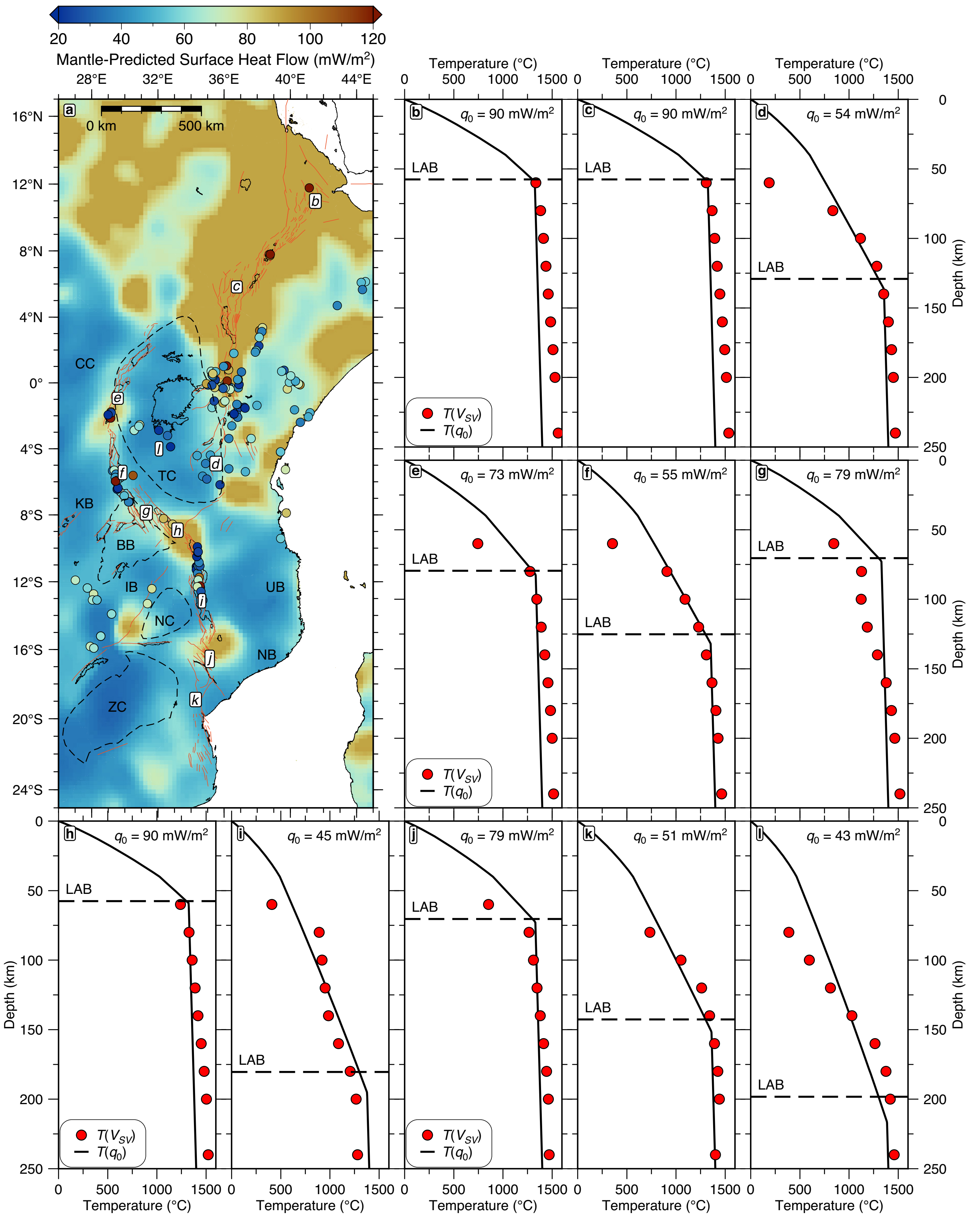

Fig. 3. Illustration of the procedure for estimating the lithosphere-asthenosphere boundary (LAB). (a) Mantle-predicted surface heat flows q_0 derived from the optimization and surface heat flow measurements (colored circles) from the compilation of Jones (2020). We do not use observed surface heat flow measurements as constraints in the optimization because we do not have estimates of crustal temperatures or details of crustal heat production, thermal conductivities, and near-surface conditions in the region that can significantly modify the mantle-predicted heat flows. Lettered boxes highlight the locations of the panels in b – l, with the letters corresponding to the panels. Full name of abbreviations: BB, Bangweulu Block; CC, Congo Craton; IB, Irumide Belt; KB, Kibaran Belt; NB, Nampula Block; NC, Niassa Craton; TC, Tanzania Craton; UB, Unango Block; ZC, Zimbabwe Craton. (b – l) Fits of theoretical steady-state continental geotherm $T(q_0)$ (black line) and the predicted temperatures ($T(V_{SV})$) estimated from the V_{SV} model of van Herwaarden et al. (2023).

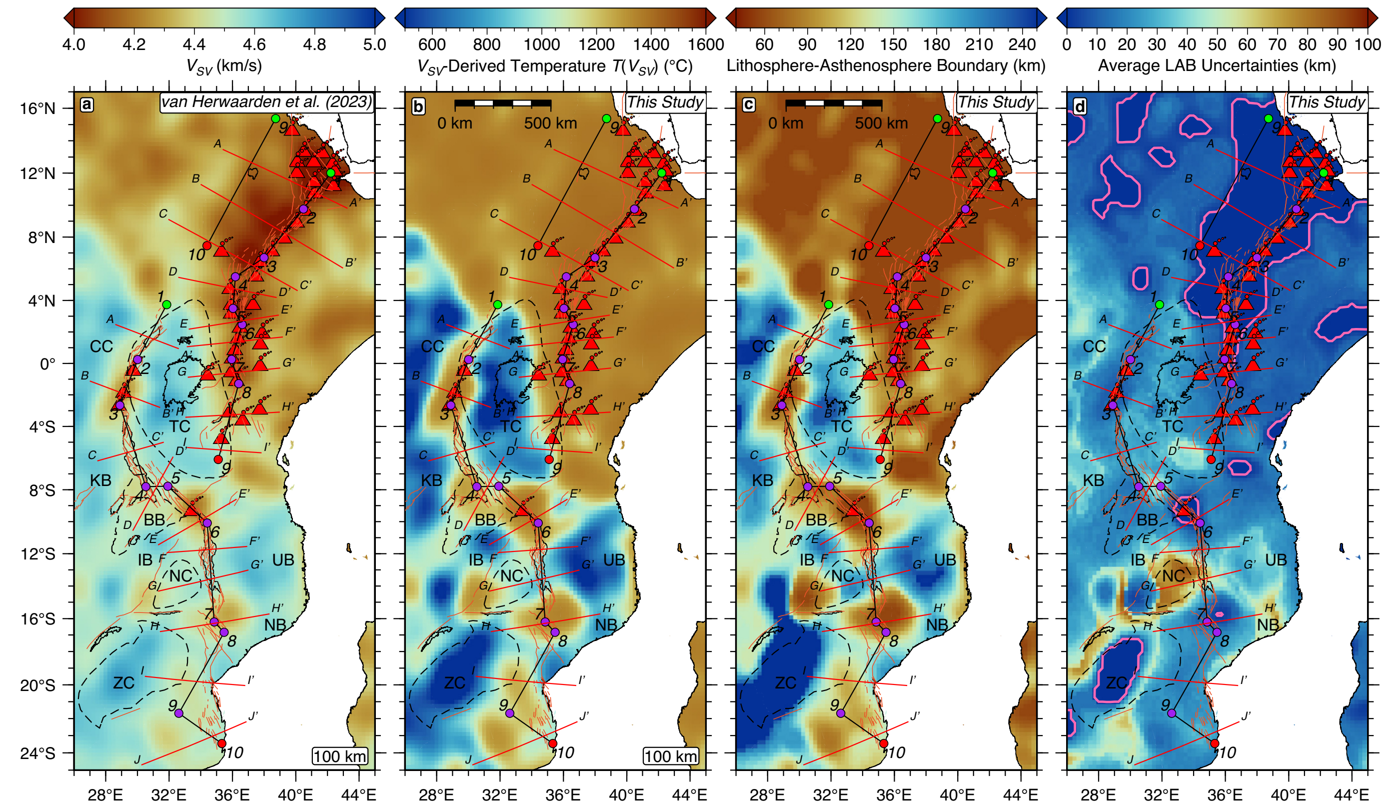

Fig. 4. (a) Wave speeds of vertically polarized S waves (V_{SV}) from the model of van Herwaarden et al. (2023) at 100 km depth. (b) Temperatures at 100 km depth derived from the V_{SV} model. (c) Lithosphere-asthenosphere boundary (LAB) derived from the temperature model. (d) Average uncertainties in the LAB model. Pink contours highlight extrema regions of the models with poorly constrained uncertainties. As explained in the text, uncertainties in these regions are probably close to zero but not exactly zero due to geologic and crustal model constraints, e.g., the LAB cannot be shallower than the Moho. Map symbols are consistent with previous figures. Full name of abbreviations: BB, Bangweulu Block; CC, Congo Craton; IB, Irumide Belt; KB, Kibaran Belt; NB, Nampula Block; NC, Niassa Craton; TC, Tanzania Craton; UB, Unango Block; ZC, Zimbabwe Craton.

(2023). We also compare our LAB model with that of Fishwick (2010) (Supplementary Data Fig. S33), which uses a similar methodology and a surface-wave tomography model of the African Plate. Cross-sectional profiles of V_{SV}, V_{SV}-derived temperatures, LAB, and our compilations of the crustal structure are shown in Figs. 5–8. Cross-sectional profile comparison with the models of Priestley et al. (2024) and Fishwick (2010) along similar profiles is shown in Supplementary Data Figs. S34–S47.

4.3. Integrated lithospheric yield strength

Using the best-fit steady-state continental geotherms ($T(q_0)$) to the V_{SV}-derived temperature estimates $T(V_{SV})$ in the model, we compute yield stress envelopes for each grid point of the model (Fig. 9) using a similar approach and thermo-rheological parameters as in Ajala et al. (2024) (Supplementary Data Table S1). The stress envelopes are then integrated to determine the lithospheric strength. The lithospheric mantle thickness is the most significant variable determining the overall strength since we adopt standard and similar rheological parameters throughout the region (Supplementary Data Table S1).

For each resulting best-fit steady-state continental geotherm $T(q_0)$ derived using the method in the previous section, we estimate the yield stress envelope and integrate it to obtain the lithospheric yield strength. For the brittle layer, the differential stress σ is given as

$$\sigma = \begin{cases} 0.85 \times P(P < 0.2\ \text{GPa}) \\ 0.5 + 0.6 \times P(\text{else}) \end{cases} \tag{16}$$

where P is the lithostatic pressure. For the ductile regime in the mantle, the creep equation gives

$$\dot{\varepsilon} = A\sigma^n d^{-m} f_{H_2O}{}^{r} e^{\left(-\frac{Q+PV}{RT}\right)} \tag{17}$$

where $\dot{\varepsilon}\left(10^{-15}\text{s}^{-1}\right)$ is the strain rate (Stamps et al., 2010), A is the pre-exponential material constant, n is the differential stress exponent, d is the grain size, m is the grain size exponent, $f_{H_2O}(1)$ is the water fugacity with exponent $r(1)$, Q is the activation energy, V is the activation volume, and $R\left(8.314\ \text{J}\,\text{K}^{-1}\,\text{mol}^{-1}\right)$ is the universal gas constant. Values for the modeling parameters are in Supplementary Data Table S1. Finally, from the resulting yield stress envelopes, we derive the yield strength $\hat{\sigma}$ via the depth z integral

$$\hat{\sigma} = \int_Z \sigma(z)dz \tag{18}$$

Fig. 9 shows the estimated strength and stress profiles at selected locations. The upper- and lower-bound estimates of the LAB (e.g., Figs. 5–8) are used to estimate uncertainties in the strength, which is shown in Supplementary Data Fig. S31. Given the simplicity of the modeling approach, the strength estimates obtained here are first-order and vary regionally, largely due to differences in lithospheric mantle thickness. Nonetheless, the values are within estimates from previous studies (e.g., Tesauro et al., 2012).

4.4. Crustal ($\boldsymbol{\beta}_{\mathbf{C}}$) and lithospheric mantle ($\boldsymbol{\beta}_{\mathbf{L}}$) thinning factors

After obtaining estimates of the LAB depths, we compute the crustal and lithospheric mantle thinning factors (Figs. 10–12). For

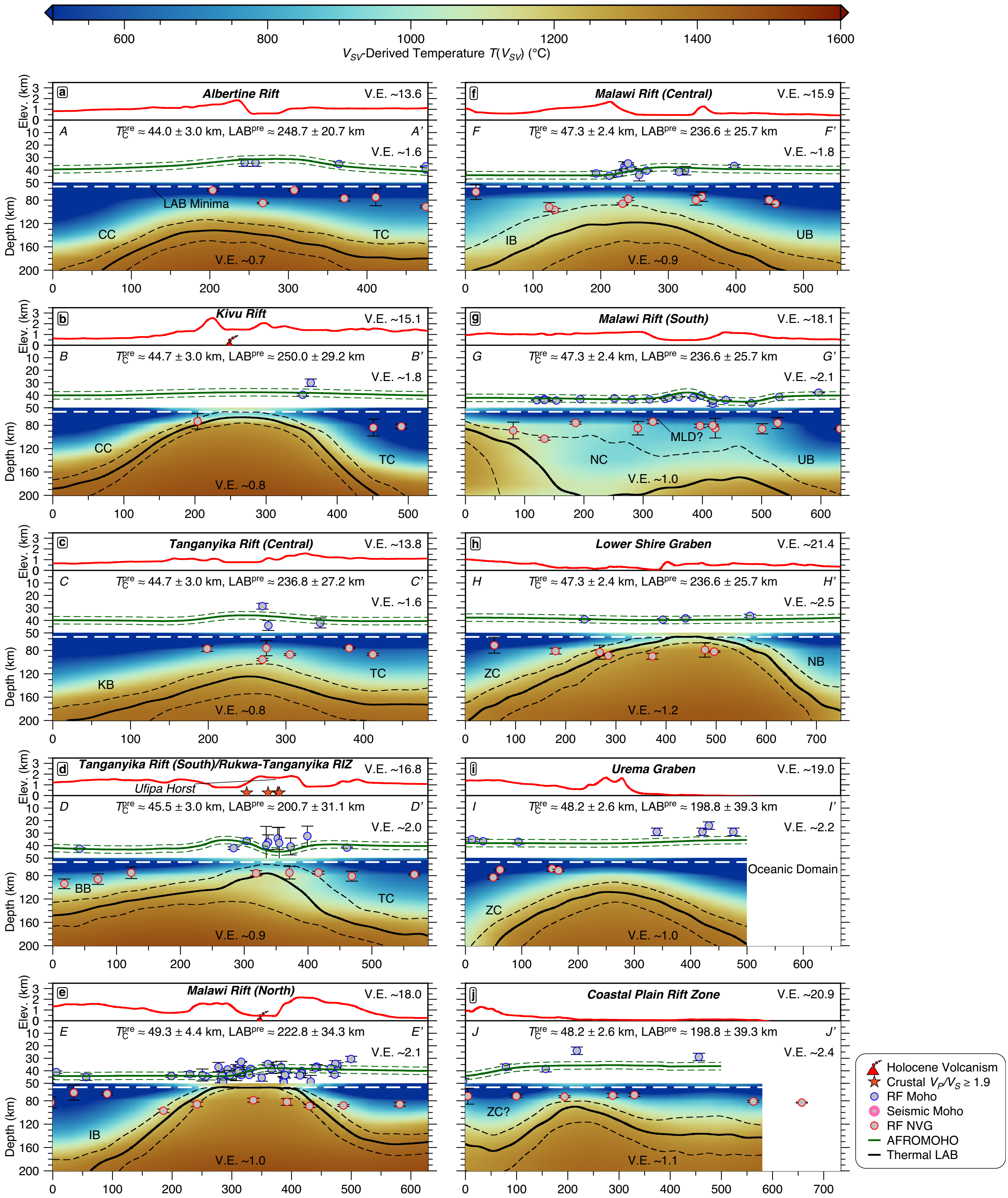

Fig. 5. Temperature and LAB models across the western branch of the EARS. (a–j) Topography (top panel) and V_{SV}-derived temperature (bottom). The red triangles represent projected volcanic centers within 50 km on either side of the profile. The red stars are projected station sites within 50 km on either side of the profile with crustal-averaged V_P/V_S ratios equal to or exceeding 1.9, indicating crustal modification by magmatism (Fig. 2c). The black line is the LAB extracted from the map shown in Fig. 4c. The green line represents Moho depths from the African Moho model (AFROMOHO). The dashed white line is the minimum permitted value of the LAB in the modeling procedure. Gray circles with blue outlines represent Moho depths from receiver function (RF) studies (Fig. 2b), projected within 50 km on each side of the profile. Gray circles with red outlines represent lithospheric negative velocity gradients (NVGs) from receiver function studies (Fig. 2d), projected within a 50 km on each side of the profile. The NVG represents the strongest negative phase following the RF Moho and is usually interpreted as the LAB or MLD. Labels indicate the estimated pre-rift crustal thickness (T_C^{pre}) and LAB (LAB^{pre}). Full name of abbreviations: BB, Bangweulu Block; CC, Congo Craton; IB, Irumide Belt; KB, Kibaran Belt; NB, Nampula Block; NC, Niassa Craton; RIZ, Rift Interaction Zone; RF, Receiver Function; TC, Tanzania Craton; UB, Unango Block; V.E., vertical exaggeration; ZC, Zimbabwe Craton.

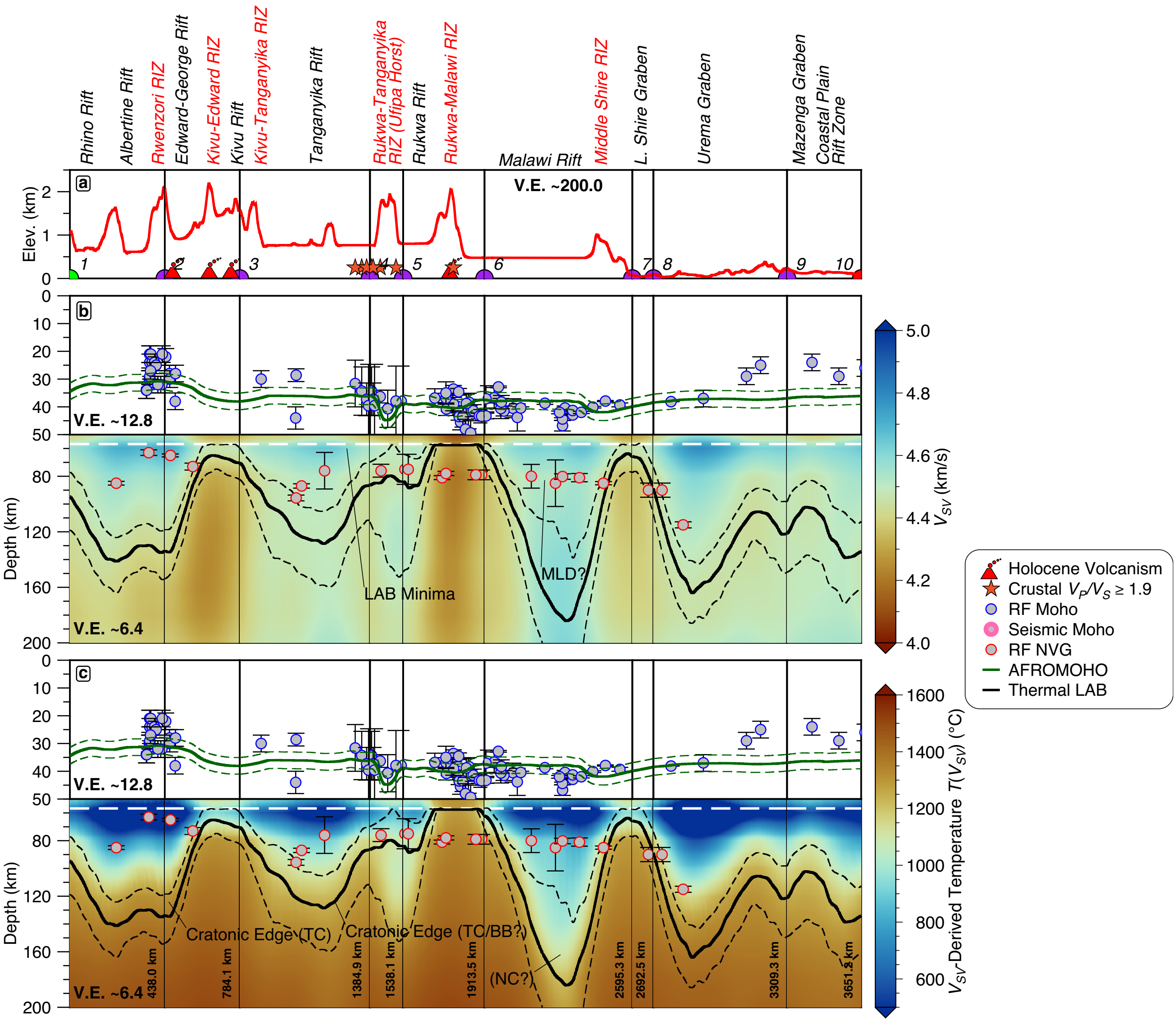

Fig. 6. Earth models from or derived from the tomography results of van Herwaarden et al. (2023) along the western branch of the EARS. (a) Topography profile (red line). The numbers next to the colored circles indicate the checkpoint locations in Figs. 1 and 2. The red triangles represent projected volcanic centers within 50 km on either side of the profile. The red stars are projected station sites within 50 km on either side of the profile with crustal-averaged V_P/V_S ratios equal to or exceeding 1.9, indicating crustal modification by magmatism. The labels at the top of the profile are the main rift segments and rift interaction zones (RIZ). (b) V_{SV}. (c) Estimated temperature model from this study. The black line is the LAB extracted from the map shown in Fig. 4c. The green line represents Moho depths from the African Moho model (AFROMOHO). The dashed white line is the minimum permitted value of the LAB in the modeling procedure. Gray circles with blue outlines represent Moho depths from receiver function (RF) studies (Fig. 2b), projected within 50 km on each side of the profile. Gray circles with red outlines represent lithospheric negative velocity gradients (NVGs) from receiver function studies (Fig. 2d), projected within 50 km on both sides of the profile. The NVG represents the strongest negative phase following the RF Moho and is usually interpreted as the LAB or MLD. Full name of abbreviations: BB, Bangweulu Block; MLD, Mid-Lithospheric Discontinuity; NC, Niassa Craton; NVG, Negative Velocity Gradient; RF, Receiver Function; TC, Tanzania Craton; V.E., Vertical Exaggeration.

the profiles along the EARS' western and eastern branches, the thinning factors are calculated as the ratio of the pre-rift crustal or lithospheric mantle thickness to the present-day thickness estimates. Our sampling locations comprise our compilations of crustal models from passive- and active-source studies, including AFROMOHO (Fig. 2b). At these same locations, we sample the sediment thickness grid whenever sediment thickness values are unavailable and our LAB model. Thus, no model projection was performed to compute the thinning factors except when estimating pre-rift thicknesses. We project the measurements (Moho and NVGs) along the profiles (Figs. 5–8) solely for illustration.

To compute the crustal (β_C) and lithospheric mantle (β_L) thinning factors, we first estimate the pre-rift crustal thickness ($T_C{}^{pre}$) and LAB (LAB^{pre}). For each along-axis profile segment j along the western and eastern branch (i.e., the numbered profiles in Fig. 1b, 2c, and 4), we define $T_C{}^{pre}{}_j$ as the maximum crustal thickness from the values projected on either side of the rift segment using a projection distance based on the across-axis profiles (i.e., the lettered profiles in Fig. 1b, 2c, and 4). The projection distance is defined as the maximum across-axis profile width on either side of the corresponding along-axis profile segment. A similar approach is used to estimate LAB^{pre}, which we pick as the maximum LAB along each along-axis segment within the distance defined by the across-rift segments. The estimated values of $T_C{}^{pre}$ and LAB^{pre} and their uncertainties are labeled on the across-rift profiles (e.g., Figs. 5, 7, and Supplementary Data Figs. S35 and S40). We thus compute the thinning factors i in each along-axis segment j as follows

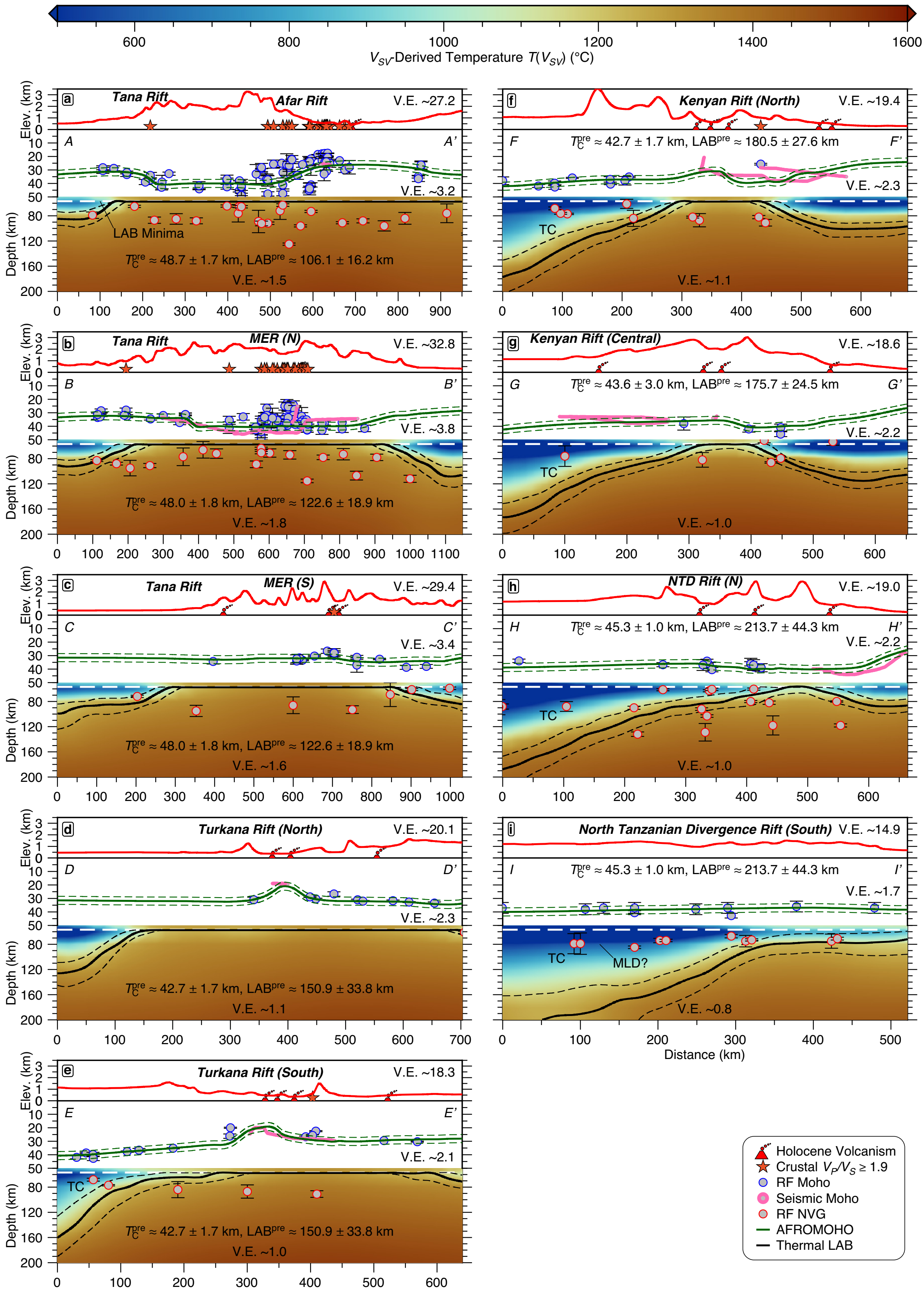

600 800 1000 1200 1400 1600
V_{SV}-Derived Temperature $T(V_{SV})$ (°C)
a Tana Rift Afar Rift V.E. ~27.2
A A'
V.E. ~3.2
LAB Minima
T_C^{pre} ≈ 48.7 ± 1.7 km, LAB^{pre} ≈ 106.1 ± 16.2 km
V.E. ~1.5
f Kenyan Rift (North) V.E. ~19.4
F T_C^{pre} ≈ 42.7 ± 1.7 km, LAB^{pre} ≈ 180.5 ± 27.6 km F'
V.E. ~2.3
TC
V.E. ~1.1
b Tana Rift MER (N) V.E. ~32.8
B B'
V.E. ~3.8
T_C^{pre} ≈ 48.0 ± 1.8 km, LAB^{pre} ≈ 122.6 ± 18.9 km
V.E. ~1.8
g Kenyan Rift (Central) V.E. ~18.6
G T_C^{pre} ≈ 43.6 ± 3.0 km, LAB^{pre} ≈ 175.7 ± 24.5 km G'
V.E. ~2.2
TC
V.E. ~1.0
c Tana Rift MER (S) V.E. ~29.4
C C'
V.E. ~3.4
T_C^{pre} ≈ 48.0 ± 1.8 km, LAB^{pre} ≈ 122.6 ± 18.9 km
V.E. ~1.6
h NTD Rift (N) V.E. ~19.0
H T_C^{pre} ≈ 45.3 ± 1.0 km, LAB^{pre} ≈ 213.7 ± 44.3 km H'
V.E. ~2.2
TC
V.E. ~1.0
d Turkana Rift (North) V.E. ~20.1
D D'
V.E. ~2.3
T_C^{pre} ≈ 42.7 ± 1.7 km, LAB^{pre} ≈ 150.9 ± 33.8 km
V.E. ~1.1
i North Tanzanian Divergence Rift (South) V.E. ~14.9
I T_C^{pre} ≈ 45.3 ± 1.0 km, LAB^{pre} ≈ 213.7 ± 44.3 km I'
V.E. ~1.7
TC
MLD?
V.E. ~0.8
Distance (km)
e Turkana Rift (South) V.E. ~18.3
E E'
V.E. ~2.1
TC
T_C^{pre} ≈ 42.7 ± 1.7 km, LAB^{pre} ≈ 150.9 ± 33.8 km
V.E. ~1.0
Distance (km)
Elev. (km)
Depth (km)
Holocene Volcanism
Crustal V_P/V_S ≥ 1.9
RF Moho
Seismic Moho
RF NVG
AFROMOHO
Thermal LAB

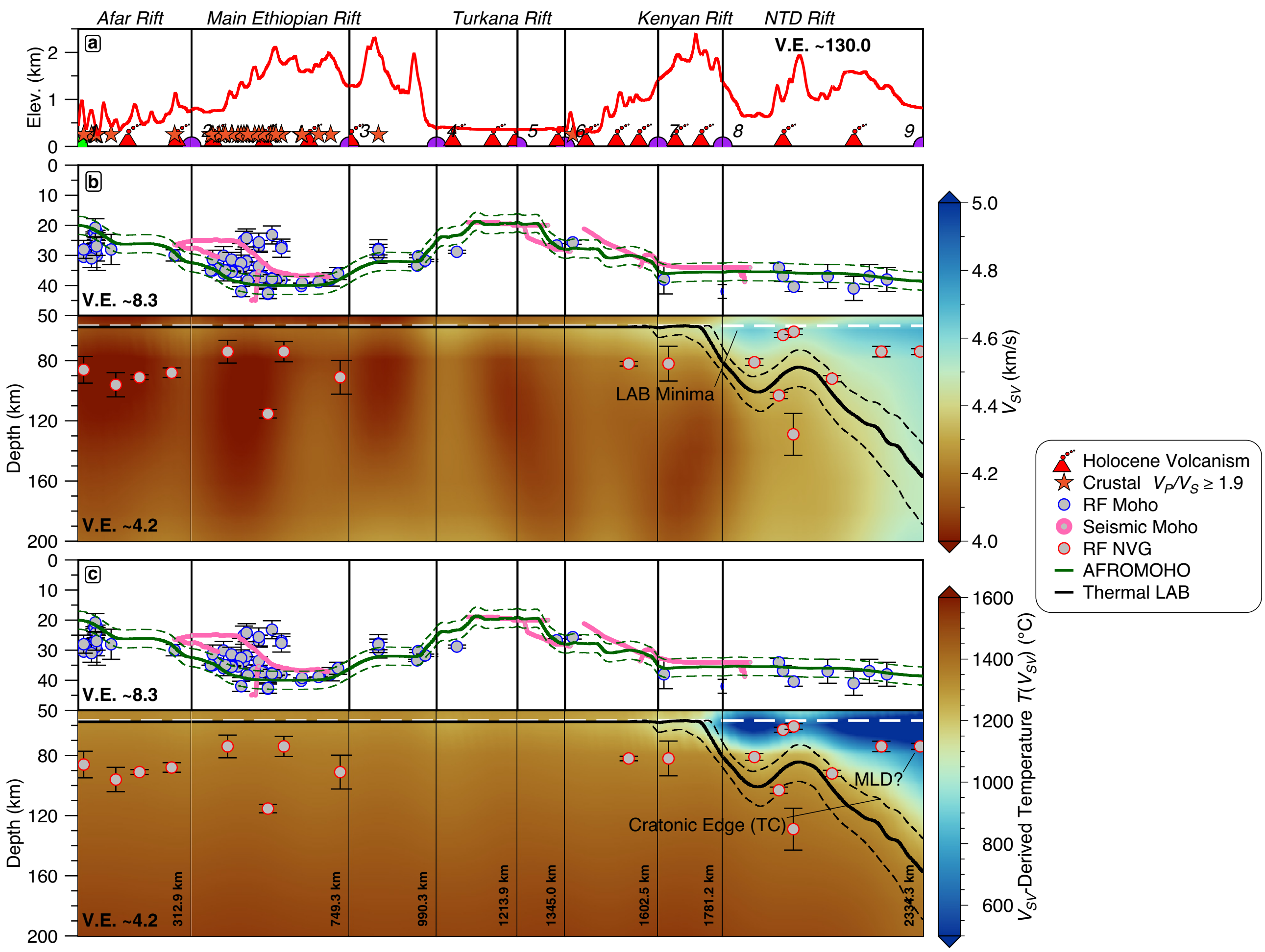

Fig. 8. Earth models from or derived from the tomography results of van Herwaarden et al. (2023) along the eastern branch of the EARS. (a) Topography profile (red line). The numbers next to the colored circles indicate the checkpoint locations in Figs. 1 and 2. The red triangles represent projected volcanic centers within 50 km on either side of the profile. The red stars are projected station sites within 50 km on either side of the profile with crustal-averaged V_P/V_S ratios equal to or exceeding 1.9, indicating crustal modification by magmatism. The labels at the top of the profile are the main rift segments and rift interaction zones (RIZ). (b) V_{SV}. (c) Estimated temperature model from this study. The black line is the LAB extracted from the map shown in Fig. 4c. The green line represents Moho depths from the African Moho model (AFROMOHO). The dashed white line is the minimum permitted value of the LAB in the modeling procedure. Gray circles with blue outlines represent Moho depths from receiver function studies (Fig. 2b), projected within 50 km on each side of the profile. Gray circles with pink outlines represent Moho depths from active source studies (Fig. 2b), projected within 50 km on each side of the profile. Gray circles with red outlines represent lithospheric negative velocity gradients (NVGs) from receiver function studies (Fig. 2d), projected within 50 km on both sides of the profile. The NVG represents the strongest negative phase following the RF Moho and is usually interpreted as the LAB or MLD. Full name of abbreviations: BB, Bangweulu Block; MLD, Mid-Lithospheric Discontinuity; NC, Niassa Craton; NVG, Negative Velocity Gradient; RF, Receiver Function; TC, Tanzania Craton; V.E., Vertical Exaggeration.

$$\beta_{\mathrm{C}ij} = \frac{{T_{\mathrm{C}}^{\mathrm{pre}}}_j}{T_{\mathrm{C}ij}} \tag{19}$$

and

$$\beta_{\mathrm{L}ij} = \frac{{T_{\mathrm{L}}^{\mathrm{pre}}}_j}{T_{\mathrm{L}ij}} = \frac{\mathrm{LAB}^{\mathrm{pre}}_j - T_{\mathrm{C}ij}}{\mathrm{LAB}_{ij} - T_{\mathrm{C}ij}} \tag{20}$$

where $T_{\mathrm{C}ij}$ are the present-day crustal thickness estimates (Supplementary Data Fig. S12). LAB_{ij} are the LAB values sampled at the exact locations as $T_{\mathrm{C}ij}$. ${T_{\mathrm{L}}^{\mathrm{pre}}}_j$ is the pre-rift lithospheric mantle thickness, and $T_{\mathrm{L}ij}$ is the present-day lithospheric mantle thickness. The $T_{\mathrm{C}}^{\mathrm{pre}}$ and $T_{\mathrm{C}ij}$ computed here account for sediment thickness (Fig. 10 and 11). Results that do not account for sediments are shown in Supplementary Data Figs. S48 and S49. For our passive

Fig. 7. Temperature and LAB models across the eastern branch of the EARS. (a–i) Topography (top panel) and V_{SV}-derived temperature (bottom). The red triangles represent projected volcanic centers within 50 km on either side of the profile. The red stars are projected station sites within 50 km on either side of the profile with crustal-averaged V_P/V_S ratios equal to or exceeding 1.9, indicating crustal modification by magmatism (Fig. 2c). The black line is the LAB extracted from the map shown in Fig. 4c. The green line represents Moho depths from the African Moho model (AFROMOHO). The dashed white line is the minimum permitted value of the LAB in the modeling procedure. Gray circles with blue outlines represent Moho depths from receiver function (RF) studies (Fig. 2b), projected within 50 km on each side of the profile. Gray circles with pink outlines represent Moho depths from active source studies (Fig. 2b), projected within 50 km on each side of the profile. Gray circles with red outlines represent lithospheric negative velocity gradients (NVGs) from receiver function (RF) studies (Fig. 2d), projected within a 50 km on each side of the profile. The NVG represents the strongest negative phase following the RF Moho and is usually interpreted as the LAB or MLD. Labels indicate the estimated pre-rift crustal thickness (T_C^{pre}) and LAB ($\mathrm{LAB}^{\mathrm{pre}}$). Full name of abbreviations: BB, Bangweulu Block; CC, Congo Craton; IB, Irumide Belt; KB, Kibaran Belt; MER (N), Main Ethiopian Rift (North); MER(S), Main Ethiopian Rift (South); NB, Nampula Block; NC, Niassa Craton; NTD Rift (N), North Tanzanian Divergence Rift (North); TC, Tanzania Craton; UB, Unango Block; V.E., Vertical Exaggeration; ZC, Zimbabwe Craton.

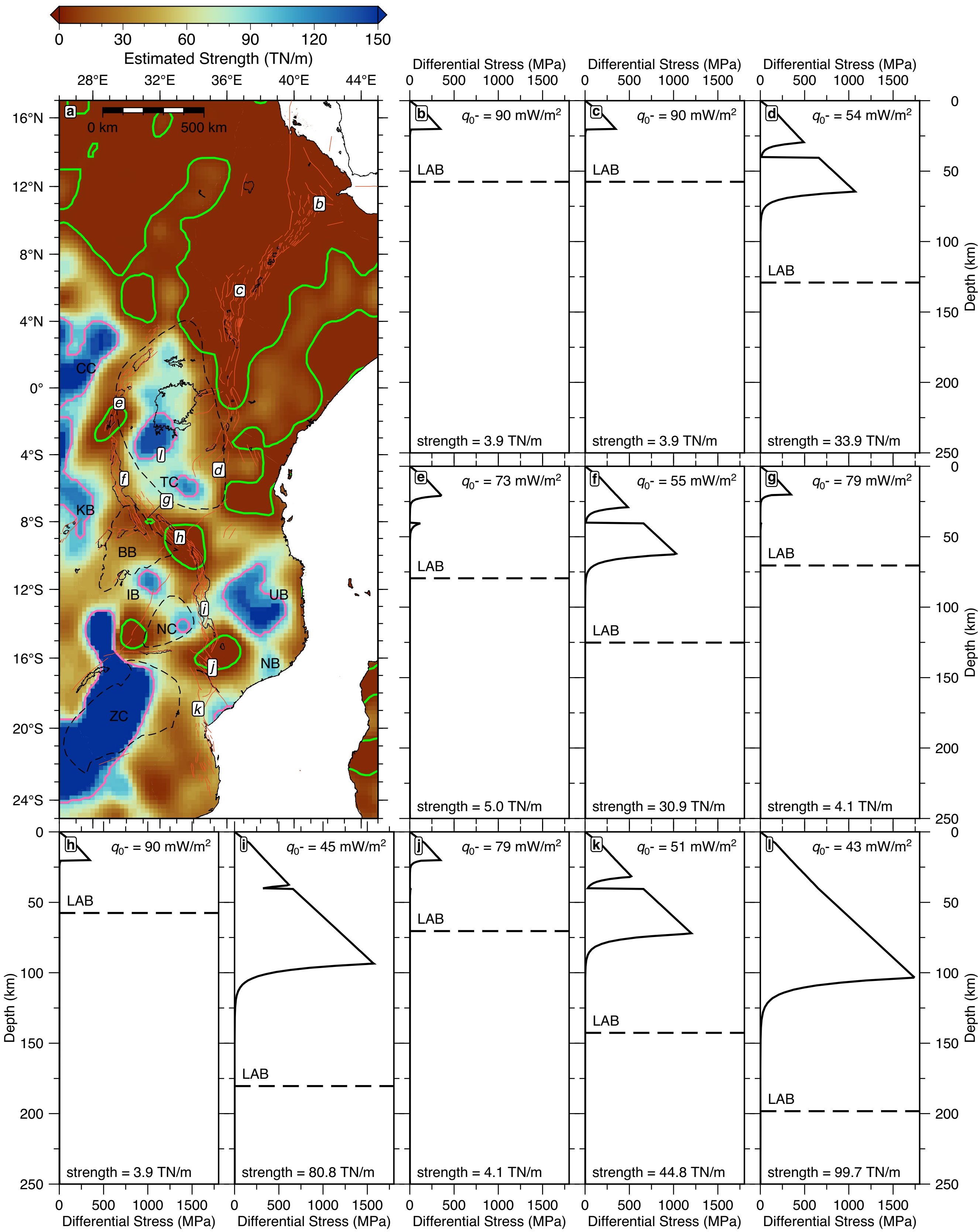

Fig. 9. Integrated lithospheric yield strength. (a) Map of the integrated lithospheric yield strength. Lettered boxes highlight the locations of the panels in b – l, with the letters corresponding to the panels. Given the simplicity of the modeling approach, the strength estimates obtained here are first-order and vary regionally, largely due to differences in lithospheric mantle thickness. Nonetheless, the values are within estimates from previous studies (e.g., Tesauro et al., 2012). (b – l) Yield stress envelopes. Dashed black line is the estimated LAB. The surface heat flow value q_0 for $T(q_0)$ (Fig. 3) is labeled at the top. The estimated lithospheric strength is labeled at the bottom. Green contours and pink contours represent the 5 TN/m and 100 TN/m, respectively. Uncertainties are shown in Supplementary Data Fig. S31.

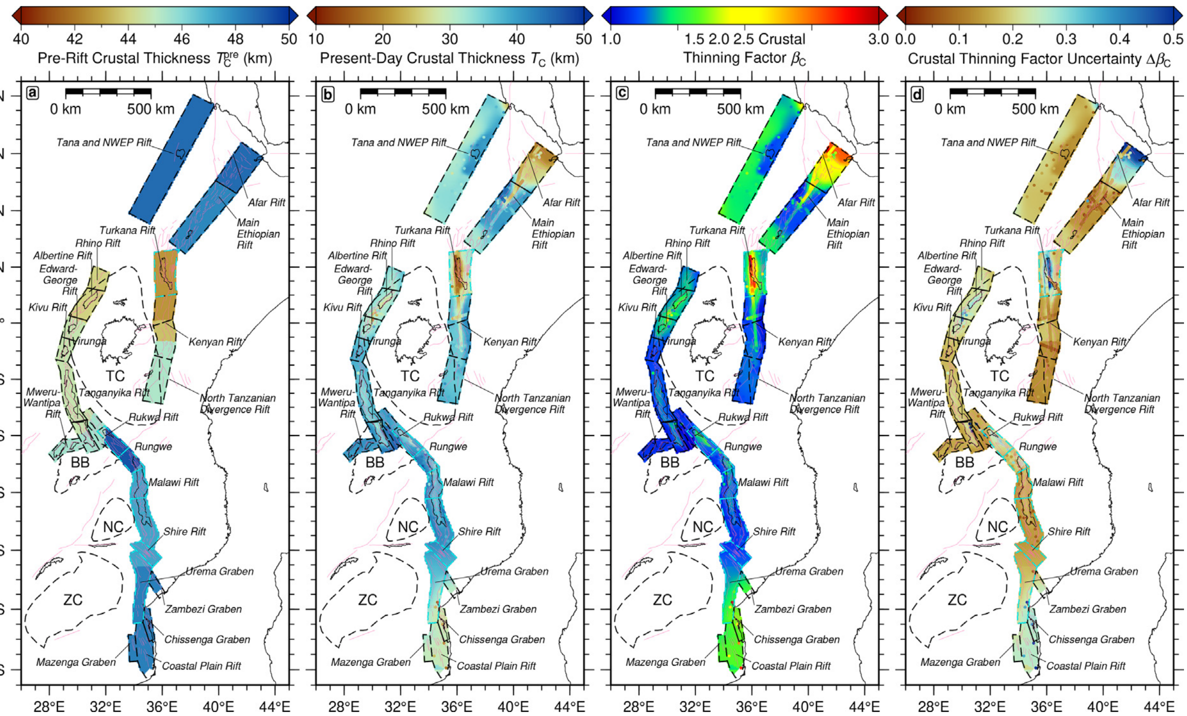

Fig. 10. (a) Pre-rift crustal thickness. (b) Present-day crustal thickness. (c) Crustal thinning factors. (d) Crustal thinning factor uncertainties. Dashed boxes highlight the region used to estimate rift-segment values in Table 1. Blue boxes are segments with inheritance. Full name of abbreviations: BB, Bangweulu Block; NC, Niassa Craton; TC, Tanzania Craton; ZC, Zimbabwe Craton. These results are provided in Ajala et al. (2026a).

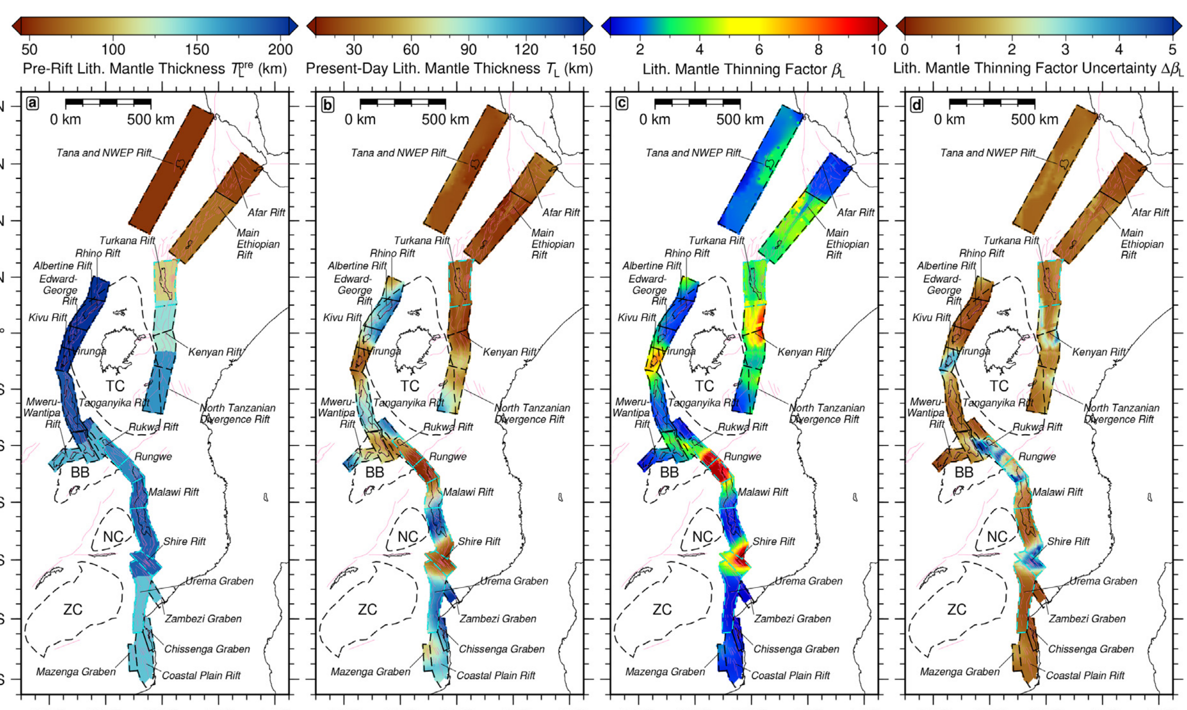

Fig. 11. (a) Pre-rift lithospheric mantle thickness. (b) Present-day lithospheric mantle thickness. (c) Lithospheric mantle thinning factors. (d) Lithospheric mantle thinning factor uncertainties. Dashed boxes highlight the region used to estimate rift-segment values in Table 1. Blue boxes are segments with inheritance. Full name of abbreviations: BB, Bangweulu Block; NC, Niassa Craton; TC, Tanzania Craton; ZC, Zimbabwe Craton. These results are provided in Ajala et al. (2026a).

source sampling locations and AFROMOHO grid locations without sediment thickness estimates, we first sample the active-source sediment thickness grid (Supplementary Data Fig. S9) and, when unavailable, use CRUST1.0 (Supplementary Data Fig. S10) to estimate the sediment thickness. Supplementary Data Fig. S12 shows the crustal thickness estimates with and without sediments.

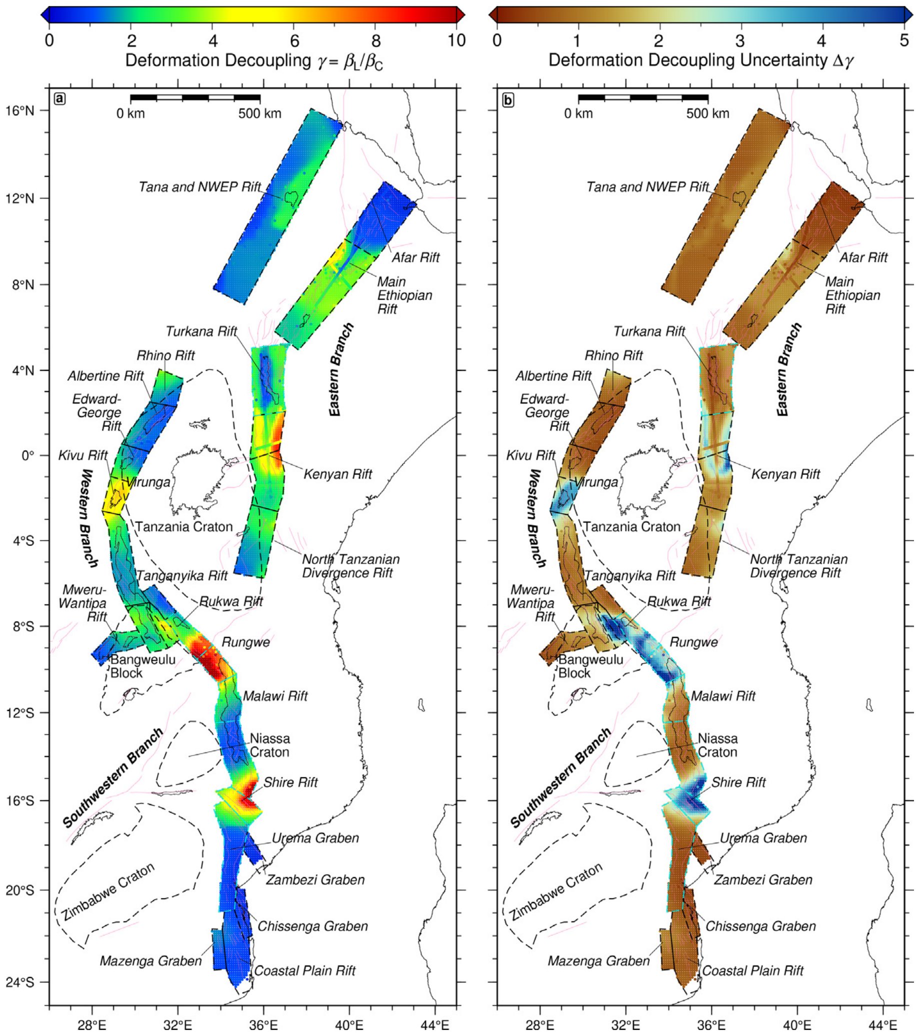

Fig. 12. (a) Deformation decoupling factors. (b) Deformation decoupling factor uncertainties. Dashed boxes highlight the region used to estimate rift-segment values in Table 1. Blue boxes are segments with inheritance. These results are provided in Ajala et al. (2026a).

We use maximum pre-rift thicknesses to prevent thinning factors from falling below unity, which would imply crustal or lithospheric thickening. In the case of the crust, this introduces the additional complexity of magmatic underplating (Thybo et al., 2000; Dugda and Nyblade, 2006). In these underplating cases, the thinning factors will be overestimated.

We account for uncertainties in the thinning factors by propagating the errors in the crustal and lithospheric mantle thickness. In general, the uncertainty in the thinning factors, for example, in the crust, is calculated as

$$\Delta\beta_{\mathrm{C}ij} = \beta_{\mathrm{C}ij}\left(\frac{\Delta T_{\mathrm{C}}{}^{\mathrm{pre}}{}_{j}}{T_{\mathrm{C}}{}^{\mathrm{pre}}{}_{j}} + \frac{\Delta T_{\mathrm{C}ij}}{T_{\mathrm{C}ij}}\right) \tag{21}$$

A similar equation is used to determine $\Delta\beta_{\mathrm{L}ij}$. Due to inherent differences in uncertainties and sample sizes across the datasets (active- and passive-source compilations and the AFROMOHO grid) used in the study, we adopt an inverse-uncertainty-weighted method to compute averages and their uncertainties. Therefore, for a particular rift segment, we calculate the average as

$$\overline{\beta_{\mathrm{C}ij}} = \frac{\sum w_{ij}\beta_{\mathrm{C}ij}}{\sum w_{ij}} \tag{22}$$

and the uncertainty in the average as

$$\Delta\overline{\beta_{\mathrm{C}ij}} = \sqrt{\frac{1}{\sum w_{ij}}} \tag{23}$$

where the weights w_{ij} are defined as

$$w_{ij} = \frac{1}{\Delta\beta_{\mathrm{C}ij}{}^{2}} \tag{24}$$

Figs. 10 and 11 show the estimated pre-rift thickness, present-day thickness, thinning factors, and uncertainties in the thinning factors for the crust and lithospheric mantle, respectively. Summary of the results for our defined rift segments (boxes in Figs. 10 and 11) is in Table 1.

4.5. Deformation decoupling (γ)

To quantitatively compare the relative amount of thinning in the crust and lithospheric mantle, we define the deformation decoupling factor γ calculated as

$$\gamma_{ij} = \frac{\beta_{\mathrm{L}ij}}{\beta_{\mathrm{C}ij}} \tag{25}$$

Values closer to unity indicate a commensurate amount of thinning in the crust and lithospheric mantle (Fig. 12). Values much greater than unity imply that the lithospheric mantle has undergone significant extension relative to the crust. Uncertainties in the decoupling factors are computed in a similar manner as described in Eq. (21). The estimation of the rift-segment average and the uncertainty in the average is also computed in a similar fashion (Eqs. (22) – (24)). Results of the deformation decoupling that do not account for sediment thickness are shown in Supplementary Data Fig. S50 and summarized in Supplementary Data Table S2. The deformation decoupling factor is a new parameter introduced in this study to quantitatively compare the amount of lithospheric mantle thinning with that of crustal thinning. However, the parameter needs to be further studied in continental extension research to place the physical intuition and implication for rifting on a more rigorous footing.

4.6. Limitations of the study

4.6.1. Lithospheric structure model coverage and source

We use as much publicly available information as possible from lithospheric structure models developed throughout the EARS. However, these models are still limited in the sampling locations they cover. For example, we do not incorporate models that sample exactly along the rift axis in some locations. At these locations, we probably underestimate thinning factors. Our active-source sediment thickness grid is sparse (Supplementary Data Fig. S9) and lacks estimates for some rift basins in the western branch and for most rift basins in the eastern branch. When these active-source-derived estimates of sediment thickness are missing, our use of CRUST1.0 may introduce errors (Supplementary Data Fig. S10). Finally, we note that our study focuses solely on seismological constraints and does not incorporate models from potential-field, petrology, or geochemistry studies that could improve the robustness of the work.

4.6.2. Choice of modeling parameters

Although we make the effort to be systematic in our approach to modeling the LAB and thinning factors, and to incorporate uncertainties whenever possible, there remain inherent limitations stemming from epistemic uncertainties regarding some lithospheric parameters. While modeling the LAB, we fit the V_{SV}-derived temperatures using a theoretical steady-state continental geotherm developed using standard assumptions about heat production and thermal conductivities in the crust and lithospheric mantle (Supplementary Data Table S1). However, we have no detailed knowledge of how these parameters vary throughout the EARS. By restricting the continental geotherms to be determined using heat flow values within the range from 30 to 90 mW/m^2, we impose an LAB minimum of 56.8 km and additionally impose an LAB maximum of 250 km based on LAB estimates from previous studies (Fishwick, 2010; Afonso et al., 2022; Priestley et al., 2024). At these extremes, it becomes difficult to estimate the uncertainties in the LAB (Fig. 4d). Our restriction of the LAB at shallower depths is informed by the regional observations of Moho depths because if the LAB becomes much shallower, then the values coincide with Moho depths (Figs. 5–8) and may even be shallower than the Moho depths, which is geologically unfeasible. We observe this exact scenario in the LAB model of Priestley et al. (2024) (e.g., Supplementary Data Figs. S39, S41, S42, S43, S46, and S47) and choose to avoid it. A similar constraint appears to be implemented in the LAB model of Fishwick (2010). However, their LAB model still sometimes coincides with Moho depths (e.g., Supplementary Data Fig. S46). Thus, the true uncertainties in the LAB model at these locations are likely closer to zero (i.e., <10 km), as values much larger than zero would imply coincidence with other lithospheric boundaries, such as the Moho. The difficulty of mapping the thermal LAB under highly warm upper-mantle conditions is documented by studies using other techniques (e.g., Rychert et al., 2012). Due to a lack of temperature estimates and knowledge of heat production and distribution in the crust, our mantle-predicted surface heat flow cannot be readily compared with surface measurements, but remains generally consistent (e.g., Fig. 3 and Supplementary Data Fig. S30). We further note that surface heat flow measurements often vary significantly over relatively short distances (e.g., Fig. 3 and Supplementary Data Fig. S30), underscoring the uncertainty and complexity of these measurements. In modeling integrated lithospheric strength, we

Table 1
Summary of crustal thinning, lithospheric mantle thinning, and deformation decoupling results in each rift segment, highlighted by dashed boxes in Figs. 10–12.

Rift Segment	N	min (β_C)	max (β_C)	w. avg(β_C)	unc(β_C)	min(β_L)	max(β_L)	w. avg(β_L)	unc(β_L)	min(γ)	max(γ)	w. avg(γ)	unc(γ)
Tana	1621	1.1079	1.9961	1.392211	0.004064	1.1213	3.9012	2.229002	0.021456	0.72337	3.5212	1.511627	0.019518
Afar	981	1.2073	2.987	1.988185	0.006435	1.4372	3.4408	1.796277	0.016341	0.50392	2.8501	0.840507	0.011051
Main Ethiopia	1567	1.0406	2.4847	1.307152	0.002835	1.7618	6.5068	3.263158	0.021476	0.78932	6.1758	1.94042	0.018788
Turkana	969	1.192	3.0355	1.790266	0.006535	2.7726	6.2085	3.304602	0.03204	0.9248	5.0923	1.410234	0.020428
N. Kenya	632	1.0311	1.8722	1.389672	0.00499	3.108	8.888	5.104884	0.048471	2.1496	8.6199	3.209344	0.044454
S. Kenya	732	1.0301	1.4641	1.292959	0.003695	2.5528	8.9181	3.51477	0.050013	1.7654	8.6574	2.544181	0.047186
NTD	451	1.1081	1.3381	1.24077	0.006066	1.3064	4.8001	2.242539	0.053904	1.1069	4.0767	1.825078	0.052993
Rhino	184	1.2151	1.4059	1.324276	0.01551	1.4691	5.0514	2.104795	0.054887	1.1473	4.0038	1.597958	0.061427
Albertine	311	1.2847	2.0988	1.399572	0.013071	1.4741	2.688	1.866048	0.02872	0.91772	2.0262	1.317483	0.032826
Edward-George	208	1.1802	2.0971	1.348449	0.014859	1.5331	5.7342	2.180361	0.050202	0.8663	4.564	1.592346	0.055879
Kivu	158	1.1587	1.2635	1.194894	0.014013	4.009	7.4794	5.815036	0.214107	3.3128	6.1892	4.893631	0.239356
N.-C. Tanganyika	428	1.0191	1.5703	1.229277	0.008919	1.7997	6.416	2.254027	0.0489	1.3148	5.4736	1.828645	0.053497
S. Tanganyika	210	1.014	1.4414	1.16445	0.011709	2.2534	3.9565	2.813781	0.103762	1.7617	3.6469	2.375048	0.112895
N. Rukwa	108	1.0484	1.422	1.144395	0.0156	1.1782	3.6275	1.535682	0.071719	1.034	3.4409	1.339191	0.082445
S. Rukwa	200	1.0316	1.6146	1.23573	0.014167	1.9807	13.916	6.691767	0.194222	1.6443	12.443	4.221852	0.208155
Ufipa Horst	113	1.0001	1.2179	1.047198	0.013469	1.8029	6.4836	2.846454	0.245352	1.5958	6.3246	2.661743	0.270637
Mweru-Wantipa	192	1.0903	1.1694	1.127714	0.011425	1.1143	2.7694	1.580658	0.047717	0.97696	2.5396	1.410981	0.057635
N. Malawi	174	1.0428	1.4692	1.216847	0.014617	4.6492	22.234	10.071066	0.182864	3.6552	21.322	7.84307	0.250802
C. Malawi	213	1.0991	1.4941	1.226453	0.010523	1.5272	7.8749	2.435845	0.087023	1.2357	6.9605	1.946269	0.088265
S. Malawi	404	1.0185	1.3375	1.168717	0.006957	1.2156	11.974	1.662397	0.048624	1.0109	10.246	1.377932	0.050217
Shire	167	1.1355	1.2749	1.194538	0.011709	2.1814	11.297	5.238766	0.219643	1.711	9.513	4.325038	0.227763
Urema	426	1.1915	3.0125	1.352859	0.009131	1.04	5.8212	1.393388	0.032584	0.34524	4.8516	0.943456	0.02949
Zambezi	67	1.3167	1.5935	1.474469	0.026399	0.9386	1.4968	1.089682	0.063133	0.59054	1.1368	0.722447	0.055267
Chissenga	112	1.6357	2.0957	1.681847	0.025236	0.99308	1.5899	1.249511	0.056822	0.59624	0.97201	0.73958	0.044908
Coastal Plain	298	1.4174	2.6778	1.615544	0.014511	1.4066	2.239	1.622745	0.051993	0.55833	1.4272	0.991162	0.040923
Mazenga	90	1.4962	1.6495	1.604492	0.026041	1.4717	2.3577	1.772366	0.114644	0.9027	1.5327	1.098217	0.089452

are primarily interested in the first-order estimate from variations in lithospheric mantle thickness, since the upper mantle is the strongest part of the lithosphere. Thus, we adopt standard and uniform rheological parameters throughout the EARS. However, we know rheology is highly variable, but we do not know the details of the variations. To summarize, our models of the LAB and, thus, surface heat flow and strength are first-order because of the standard assumptions made about the thermo-rheological parameters. As detailed knowledge of the variations of these parameters across EARS becomes available, these models should be improved.

4.6.3. Crustal and lithospheric mantle pre-rift thicknesses

The thinning factors depend strongly on the pre-rift crustal and lithospheric mantle thicknesses, which are difficult to constrain due to the region's complex geologic history. While we have good constraints on the present-day thicknesses, the pre-rift values remain highly uncertain. For example, our systematic approach of selecting the maximum crustal thickness and LAB values from the unrifted areas implies that we sometimes use cratonic crustal and LAB values for rift segments within mobile belts, and thus assume similar lithospheric thickness between the craton and mobile belts at the time of rifting. When this assumption is false, we will have overestimated our thinning factors. We also do not account for magmatic underplating in the crust, which would potentially reduce our estimates of crustal thinning factors, particularly along the eastern branch rifts. To summarize, several geological factors, including inheritance, underplating, and complex tectonic history, will significantly affect the pre-rift crustal and lithospheric mantle thicknesses presented here.

5. Results

Fig. 4 shows the V_{SV} and V_{SV}-derived mantle temperatures at 100 km depth, along with the LAB and its uncertainty. The V_{SV} of van Herwaarden et al. (2023) (Fig. 4a) shows well-defined structural heterogeneities, with low upper-mantle V_{SV} along a significant portion of the western branch, even outside the localized volcanic centers in Rungwe and Virunga. The estimated temperature model and lithosphere-asthenosphere boundaries (LAB) mimic features in the V_{SV} (Fig. 4b and c). Where the V_{SV} values are low, the temperature estimates are high, and the LAB is shallow, and vice versa.

We present across- and along-axis profiles of temperature (Figs. 5, 6c, 7, and 8c) and V_{SV} (Figs. 6b and 8b, Supplementary Data Fig. S35, and Supplementary Data Fig. S40) models, with the LAB along the western and eastern branches of the EARS. We also include the crustal thickness estimates, sites with crustal-averaged V_P/V_S ratios equal to or exceeding 1.9, and negative velocity gradients (NVG) projected within 50 km on both sides of the profile. There is a good correlation between the thermal LAB and the shear wave speeds and temperature models. We observe unusually shallow LABs in the western branch, with steep topography against the cratonic edges (Figs. 5 and 6). The LAB beneath the eastern branch is more uniform, mostly very shallow north of the North Tanzanian Divergence Rift, but becomes deeper as the profile approaches the edge of the Tanzania Craton (Figs. 7 and 8). The NVGs derived from receiver functions do not always coincide with negative gradients in wave speeds or positive gradients in temperatures in the model (Figs. 5–8). They are only sometimes consistent with the thermal LAB (Figs. 5–8). However, the MLDs in regions of thicker lithospheric mantle and the cratons are well correlated with the positive temperature gradients (Figs. 5, 6c, 7, and 8c) and negative velocity gradients (Figs. 6b and 8b) in the model. A comparison with the results of Priestley et al. (2024) and Fishwick (2010) (Supplementary Data Figs. S34–S47) shows that the NVGs have the highest correlation with the V_{SV} of van Herwaarden et al. (2023) and the temperature and thermal LAB that we herein derive from the model. However, in general, our thermal LAB has similar trends to those of Priestley et al. (2024) and Fishwick (2010) (Supplementary Data Figs. S44–S47). The estimated strength is lower along rift segments and higher in cratonic areas (green and pink contours in Fig. 9). The weakest areas appear to be along much of the eastern branch, in localized volcanic centers along the western branch, south of the Malawi rift, and in the Ufipa Horst (green contours in Fig. 9a). In these sections, the strength is within estimates of far-field tectonic stresses (Buck, 2004) (~5 TN/m; green contours in Fig. 9a). The estimated lithospheric strength is also generally consistent with previous studies (Tesauro et al., 2012).

Figs. 10 and 11 Show the thinning factors for the crust and lithospheric mantle, respectively. the maximum thinning factors along the western branch, with values exceeding 1.5, are in the edward-george, albertine, and rhino rifts, along-axis of the tanganyika rift, the southern Rukwa rift, northern Malawi rift, and along-axis of the Malawi rift, and in the Mozambique Coastal plain from the Urema Graben southward (Fig. 10c). The highest overall crustal thinning factor of ~3 is observed in the Urema Graben using crustal thickness estimates from Sabattier and Nyblade (2025) (red circles in the Mozambique Coastal Plains in Fig. 10c). The Albertine and Edward-George rifts also have maximum crustal thinning factors that exceed 2 (Fig. 10c). Along the eastern branch, the highest crustal thinning is observed along the axes of the Kenyan and Turkana rifts, in the southern section of the Main Ethiopian rift, in much of its axial region, and in Afar. The highest overall crustal thinning factor is observed beneath Turkana (~3, Fig. 10c). The crustal thinning factors are generally higher along the eastern branch than the western branch (Fig. 10c).

Along the western branch, the highest lithospheric mantle thinning factors are observed in the volcanic provinces (Virunga and Rungwe), the Ufipa Horst, the southern Malawi rift, and the Shire rift. The overall highest lithospheric mantle thinning factor (~22) along the western branch is observed in the Rungwe Volcanic Province in northern Malawi (Fig. 11c). Along the eastern branch, the highest lithospheric mantle thinning factor is observed along the northern segment of the Kenyan rift, beneath the eastern flank where values reach ~9 (Fig. 11c). We note, however, that some of the uncertainties are also high at these locations (Fig. 11d). The lithospheric mantle thinning factors are generally higher along the western branch than in the eastern branch (Fig. 11c). In both the eastern and western branches, the lithospheric mantle thinning factors are generally higher than the crustal thinning factors (Figs. 10 and 11).

Fig. 12 shows the deformation decoupling parameter, which compares the relative amounts of lithospheric mantle thinning and crustal thinning, along with their uncertainties. Outside the localized volcanic centers (Rungwe and Virunga) and in the Ufipa Horst, the southern segment of the Malawi rift, and the Shire rift, the deformation decoupling factor is generally less than 3. The deformation decoupling factor is also generally less than 3 for much of the eastern branch outside of the flanks of the northern Kenyan rift (Fig. 12a). The deformation decoupling factors are much higher in the western branch where they reach a value of 21.3 in Rungwe Volcanic Province in northern Malawi compared to the eastern branch where they reach a maximum of 8.7 at the eastern flank of the Kenya rift. We again note that some of the uncertainties are also high at these locations (Fig. 12b). Overall, these results indicate that fluid and magmatism have modified the crust in the EARS. However, unlike the eastern branch, the amount of lithospheric mantle thinning at some segments of the western branch is anomalously high, given the relatively minor amount of crustal thinning, such as the localized volcanic centers

(Rungwe in northern Malawi and Virunga in Kivu) and in the Ufipa Horst, the southernmost segment of the Malawi rift, and the Shire rift.

6. Discussion

6.1. Comparison to previous studies

Our analysis adopts the thermal definition of the LAB, given by the 1300 °C isotherm (Ajala et al., 2024). This definition, based on temperature, differs from others, such as impedance contrast (e.g., NVG) used in the receiver function technique, as it is not always associated with significant changes in velocity, nor with thermobarometers derived from erupted mantle material (i.e., "chemical" LAB). When fitting steady-state geotherms to the temperature model, the maximum surface heat flow of 90 mW/m^2 set in the optimization procedure yields observed LAB minima of approximately 56.8 km along the profiles (Figs. 5–8). Without this restriction, the estimated thermal LAB could fall within the range of Moho depths estimated from receiver functions, such as in the results of Priestley et al. (2024) (Supplementary Data Figs. S46 and S47). The effect of this modeling choice is more apparent along the eastern branch, where the thermal LAB appears flat along most of the northern segment. A similar effect is also observed in the LAB map of Fishwick (2010) (Supplementary Data Figs. S46 and S47) and other thermal LAB maps for the eastern branch of the EARS presented in the literature (e.g., Afonso et al., 2022). Studies using receiver functions also note the difficulty of mapping the LAB along the rift axis where the subsurface temperatures are highest, such as in the eastern branch (Rychert et al., 2012).

A qualitative comparison of negative velocity discontinuities (velocity decrease with depth or temperature increase with depth) mapped from receiver functions (NVGs) and the thermal LAB only shows correlation at some of the rift segments (Figs. 5–8 and Supplementary Data Figs. S34–S47). The NVG locations do not always coincide with the LAB in the model and are generally shallower in the western branch than in the eastern branch. Along the western branch, the NVGs appear mainly within a relatively narrow range of 70 to 90 km depth and continue laterally into the cratonic regions that flank the rifts, implying a well-defined 'inherited' (i.e., pre-rift) structure at those depths within the lithosphere, possibly related to MLDs (Fu and Li, 2024). Although we observe high-to-low seismic wave-speed changes at the NVG locations in the V_{SV} model of van Herwaarden et al. (2023), these contrasts are not always apparent (e.g., Supplementary Data Fig. S35). Since receiver function data tend to have higher vertical resolution and are sensitive to regions with significant impedance contrasts (product of density and seismic wave speed), areas in the tomographic model that lack prominent wave-speed changes at the NVG depths may involve density contrasts. Some mineral physics models also suggest that the effect of melt removal or addition is greater on density than on shear wave speeds (e.g., Priestley and McKenzie, 2006). Therefore, some of the NVGs in the western branch with no apparent velocity changes could still be related to layers of melt lenses in the uppermost mantle (Fu and Li, 2024; Legre and Olugboji, 2025). The NVGs along the eastern branch are more scattered and are primarily located within the asthenosphere, as indicated by the thermal LAB derived from several tomographic models (Supplementary Data Fig. S47). Thus, if they are also associated with areas of significant melt concentration, the depth-range scatter could be due to convective currents. The MLDs have also been noted to possibly represent regions of increased water content in the mantle (Fu and Li, 2024). The velocity discontinuities may also be unresolved in the relatively long-period regional tomography models, as receiver functions tend to have higher vertical resolution.

The study closest in scope to the current research is by Hopper et al. (2020) in the northern Malawi Rift. They used receiver functions to produce crustal and lithospheric mantle thickness maps, compute their thinning factors, and find pronounced lithospheric mantle thinning factors exceeding 4 in the northern Malawi rift, similar to our result (Fig. 11c). Due to the significant amounts of thinning of the lithospheric mantle compared to the crust (highly decoupled deformation), they argue that mechanical thinning alone cannot create such a thin lithospheric mantle and propose thermochemical erosion of weakly-fusible lithospheric mantle without significant melt generation. The intense lithospheric thinning in northern Malawi is also supported by the gravity-based study of Njinju et al. (2019). Based on our results along the western branch, the deformation decoupling observed at the northern Malawi Rift may be more prevalent in the region than previously thought, as we also make similar observations in Virunga at the Kivu Rift and even outside volcanic centers such as the Ufipa Horst, the southern segment of the Malawi Rift, and the Shire Rift (Figs. 5, 6, 10–12). In these regions without surface volcanism, we propose that most of the melt generated by the thinned mantle lithosphere may not have reached the surface (e.g., Ajala et al., 2024; Kolawole and Ajala, 2024).

6.2. Necking of the lithospheric mantle beneath evolving magma-poor and magma-rich rifts

6.2.1. Evolution of lithospheric thinning styles during the early phases of continental rifting

Within the scope of our compiled datasets and analysis, our models offer an opportunity to compare lithospheric thinning styles between incipient magma-poor and magma-rich rift settings, as well as the more evolved rift segments of similar magmatic associations. The Tana and Northwest Ethiopian Plateau (NWEP) Rift in Ethiopia (Fig. 7a–c), a volcanic zone with diffuse faulting and a poorly developed rift basin that lacks a border fault (Chorowicz et al., 1998), could be regarded as a juvenile magma-rich rift in comparison to the relatively more mature Main Ethiopian Rift, Kenya Rift, or Turkana Rift. Similarly, the southern Malawi Rift (Fig. 5g) is a relatively less developed, juvenile, magma-poor rift compared to the northern Malawi Rift (Fig. 5e) and other segments of the western rift branch (Scholz et al., 2020; Kolawole et al., 2021b). Our results indicate that a mildly thinned lithospheric mantle, with little or no crustal thinning, underlies the central section of the Southern Malawi Rift (Figs. 5, 10c, and 11c), suggesting a very low degree of deformation decoupling (γ = 1.7, Fig. 12a), consistent with a coupled thinning style. The Tana and NWEP Rift zone exhibits considerably eroded mantle lithosphere and thinned crust (Figs. 7a, 10c, and 11c), indicating a low deformation decoupling ($\gamma < 3$, Fig. 12a), consistent with a coupled thinning style. Excluding the instances of inheritance of thinned lithospheric mantle, we infer that magma-poor and magma-rich rifts initially accommodate coupled thinning of the crust and lithospheric mantle in the earliest phase of extension, but with varying intensities. However, with progressive extension, magma-poor rifts may transition into decoupled thinning ($\gamma \gg 3$) in the event of lithospheric foundering and/or significant infiltration of low volume melts into the lithospheric mantle, whereas magma-rich rifts likely persist with more coupled thinning ($\gamma < 3$) driven by prolonged voluminous magmatism that allows for both thermal erosion of the lithospheric mantle and thermomechanical weakening and extension of the crust through diking and volcanism (Buck et al., 1988; Achauer et al., 1992; Buck 2004; Bastow et al., 2011). An exception to this model of temporal evolution of thinning styles may be rifts that develop in cratons; an example of this is the evolving Eyasi Rift in the North Tanzanian Divergence Zone of the eastern branch, where previous gravity-based models (Fletcher et al., 2018) suggest predominance of decoupled thinning, given by a significantly thinned lithospheric mantle and a mildly thinned crust.

6.2.2. Implications for progressive strain localization in thick continental lithosphere

Our estimates of crustal and lithospheric mantle thinning factors reveal intriguing magnitudes of lithospheric mantle necking beneath both the eastern (magma-rich) and western (magma-poor) branches ($\beta_L > 2$), suggesting that significant strain localization already exists at depth beneath the evolving rifts. Studies of crustal necking at rifted margins suggest that the crust is necked when the crystalline crust has been thinned to ~10 km thickness or more than half of the initial crustal thickness (Sutra et al., 2013; Chenin et al., 2018). However, there is a limited understanding of necking in the lithospheric mantle, and even less so from observations in active rifts. Here, along the juvenile yet evolving rifts of the East African Rift System, our results indicate widespread necking of the mantle lithosphere ($\beta_L > 2$). Thus, given the available data at the time of this study, the dearth of necked crust (areas with $\beta_C > 2$) along the rift system implies that the necking of the lithospheric mantle probably precedes crustal necking along evolving continental rifts.

Compared to the eastern branch, the western branch of the EARS has segments with unusually high deformation decoupling factors, in which the amount of crustal thinning is marginal relative to the amount of lithospheric mantle thinning. These areas include localized volcanic centers (Rungwe in northern Malawi and Virunga in Kivu) and the Ufipa Horst, the southernmost segment of the Malawi rift, and the Shire rift (Fig. 12a). Excluding rift segments close to the Rungwe Volcanic Province, which have the highest decoupling factor, and Virunga, the other regions are not associated with volcanism. As noted by Hopper et al. (2020), it is doubtful that the lithospheric mantle thinning factors in the northern Malawi rift are due to thinning alone, considering that the crust has only experienced relatively minor thinning. Receiver function studies by Hodgson et al. (2017) find high crustal-averaged V_P/V_S ratios exceeding 1.9 in the southern Tanganyika rift and Rukwa-Tanganyika RIZ (Fig. 2c), which was corroborated by a recent crustal anisotropy study (Ajala et al., 2024) and spatiotemporal seismicity analysis (Kolawole and Ajala, 2024) to be indicative of melt emplacement in the uppermost mantle and lower crust. Although these regions lack volcanism, the crust is likely modified and weakened at depth by melt and volatiles, and questions remain on how a considerable portion of the lithospheric mantle was lost. In contrast, thermal erosion by the African Superplume is responsible for the thinning of the lithospheric mantle along the eastern branch.

Possible explanations for the significant loss of the lithospheric mantle along segments of the magma-poor western branch are inheritance of past rifting events, lithospheric foundering, lithospheric delamination, and deep melt-induced shear lubrication. These processes likely worked together to create the current rifting style observed today. First, we note that regions with anomalous decoupling in the western branch are located within or near rift segments with inherited structures (blue dashed polygons in Figs. 10–12). Thus, the correlation suggests that inheritance likely enhanced lithospheric mantle thinning. The geochemistry of lava along the EARS in the Rungwe and Virunga Volcanic Province exhibits a signature of mixing between lithospheric mantle and asthenospheric melts. A result that can be explained by metasomatism due to the interaction of melt and volatiles, sourced from the African superplume, with peridotite in the lower lithosphere, causing the crystallization of pyroxenites (Furman, 2007; Furman et al., 2016; Rooney, 2020; Pitcavage et al., 2023; Innocenzi et al., 2024). As the pyroxenite-bearing lithology is denser than the underlying asthenosphere, gravitational instabilities can trigger lithospheric foundering (Aktag et al., 2024). The elevated LAB, i.e., a decrease in lithospheric mantle thickness resulting from the foundering of the lower lithospheric mantle, may generate melts by exposing the upper lithospheric mantle to warmer asthenospheric temperatures. The interaction between the asthenospheric mantle and the MLD can also cause lithospheric delamination (Fu and Li, 2024). In the across-rift profile of the southern Tanganyika and Rukwa-Tanganyika RIZ (Fig. 5d), the NVGs are coincident with the thermal LAB at the thinnest part of the lithospheric mantle and with sharp positive gradients in the temperature field on the flanks within the Bangweulu Block and the Tanzania Craton. Thus, the lithospheric mantle in the region could have been lost from foundering or delamination along the MLD. We observe a similar situation in the across-rift profiles of the northern Malawi rift (Fig. 5e) and Lower Shire Graben (Fig. 5h). In these other rift segments, inheritance and foundering may have assisted with the lithospheric mantle thinning as noted by the significantly shallower LABs. These interpretations support recent observations of sunken lithospheric mantle in the lower mantle uncorrelated with subduction events and possibly related to foundering or delamination (Schouten et al., 2024). An implication of the sudden loss of lithospheric mantle is thermal isostasy, which can cause surface uplift and has been proposed by Ajala et al. (2024) to be a contribution to the high elevations observed in the Ufipa Horst (Fig. 5d). The resulting LAB topography includes steep edges (e.g., Figs. 5 and 6) that facilitate the upward migration of melts and volatiles. These melts can lubricate the ductile shear zones that form the roots of the rift border-faults, thereby increasing localized viscous shear strain and further promoting the thinning of the lithospheric mantle (Kelemen and Dick, 1995; Holtzman and Kendall, 2010; Montesi, 2013). Small-scale convective currents generated at these steep LAB boundaries may also facilitate weakening. In the central section of the southern Malawi rift (Fig. 5g), the MLD may play a role in decoupling the lithosphere by acting as a horizontal shear zone, allowing the lithosphere above the MLD to accommodate deformation.

Lithospheric necking has been shown to be a crucial dynamic softening mechanism that drives strain localization and facilitates lithospheric rupture during tectonic extension (Brune et al., 2012, 2023). Based on the significantly weakened (on the order of far-field stresses ~5 TN/m) lithosphere along the rifts (Fig. 9), we propose that, if the current force balance along the East African Rift System is maintained, the rifts are primed to progressively transition to the later phases (crustal necking and onward) of continental extension as noted by numerical modeling studies (Buck et al., 1988; Buck, 2004). Altogether, these observations provide compelling insights into the styles of lithospheric thinning at evolving divergent plate boundaries, particularly in the presence of minor or voluminous magmatic input. We propose that as magma-poor rifting of thick continental lithosphere progresses, significant strain is taken up at depth in the lower lithospheric mantle and is compounded by inherited thinning and/or lithospheric foundering and delamination, such that the crust and ubiquitously strong uppermost lithospheric mantle experience relatively minor thinning. In contrast, plume-driven erosion of the lithospheric mantle and the ascent of voluminous melt facilitate significant thermal weakening and extensional strain in the crust and lithospheric mantle of magma-rich rifts.

7. Conclusion

We conducted a comparative multiscale study of continental rifting at the crustal and mantle scales along the magma-poor western branch and the magma-rich eastern branch of the EARS, using one of the most up-to-date and highest-resolution anisotropic shear-wave-speed models of the African Plate and compilations of lithospheric-structure models from active and passive seismic studies. The new wave speed model reveals delimited crustal heterogeneities, providing a more detailed view of the rift structure along the western branch than previous models developed for the region. We use this model to estimate the region's mantle temperatures and the LAB. By compiling crustal thickness estimates, we computed the crustal and lithospheric mantle thinning factors, as well as the deformation decoupling parameters, defined as the ratio of the lithospheric mantle to crustal thinning factors, for both the western and eastern branches.

Our results show widespread significant thinning of the lithospheric mantle across the East African Rift System, and given the effect on the highly diminished strength of the lithosphere (as low as ~5 TN/m, which is the order of far-field plate tectonic stresses, in many segments), we propose that the rift system is primed to progressively transition to the later phases of continental extension. Notably, we find anomalously high deformation decoupling values along segments of the western branch, indicating a severely thinned lithospheric mantle underlying a relatively unstretched crust in regions of limited magmatic input. To explain the decoupled thinning in magma-poor rifts lacking volcanism, we propose inherited thinned lithospheric mantle, melt-induced lubrication of ductile mantle-rooting faults, and lithospheric mantle foundering and delamination along mid-lithospheric discontinuities. Decoupled thinning may be an essential lithospheric deformation style in evolving magma-poor divergent plate boundaries, whereas their magma-rich counterparts exhibit more uniformly coupled thinning, addressing an age-old question: how does progressive tectonic extension in old, cold continental lithosphere initiate the transition to late-stage rifting?

Data availability

Computer programs and files to reproduce our results and figures are publicly accessible on Zenodo at https://doi.org/10.5281/zenodo.20788373 (Ajala et al., 2026b). The new LAB model can be downloaded from Zenodo at https://doi.org/10.5281/zenodo.20788317 (Ajala et al., 2026c) and will be made available on EarthScope. Compilations of lithospheric structure models from the active and passive source studies and the thinning factors can also be found on Zenodo at https://doi.org/10.5281/zenodo.20788349 (Ajala et al., 2026a).

CRediT authorship contribution statement

Rasheed Ajala: Writing – review & editing, Writing – original draft, Visualization, Validation, Supervision, Software, Resources, Project administration, Methodology, Investigation, Funding acquisition, Formal analysis, Data curation, Conceptualization. **Folarin Kolawole:** Writing – review & editing, Visualization, Validation, Supervision, Resources, Project administration, Investigation, Funding acquisition, Data curation, Conceptualization. **Jean-Joel Legre:** Writing – review & editing, Data curation. **Tolulope Olugboji:** Writing – review & editing, Data curation. **Dirk-Philip van Herwaarden:** Writing – review & editing. **Andreas Fichtner:** Writing – review & editing.

Declaration of competing interest

The authors declare that they have no known competing financial interests or personal relationships that could have appeared to influence the work reported in this paper.

Acknowledgements

We are extremely grateful to the Associate Editor, Mathew Domeier, Zhong-Hai Li, and three anonymous reviewers, for their thoughtful and thorough critique, which helped us significantly improve our manuscript. We plotted all figures using the Generic Mapping Tools (Wessel et al., 2019). R. Ajala was supported through the NSF Earth Sciences Postdoctoral Research Fellowship Award 2403573.

Appendix A. Supplementary data

Supplementary data to this article can be found online at https://doi.org/10.1016/j.gsf.2026.102396.

References

Accardo, N.J., Gaherty, J.B., Shillington, D.J., Hopper, E., Nyblade, A.A., Ebinger, C.J., Scholz, C.A., Chindandali, P.R.N., Wambura-Ferdinand, R., Mbogoni, G., Russell, J. B., Holtzman, B.K., Havlin, C., Class, C., 2020. Thermochemical modification of the upper mantle beneath the northern Malawi Rift constrained from shear velocity imaging. Geochem. Geophys. Geosyst. 21, 1–19.

Achauer, U., Maguire, P.K.H., Mechie, J., Green, W.V., Group KRISP Working, 1992. Some remarks on the structure and geodynamics of the Kenya Rift. Tectonophysics 213, 257–268.

Accardo, N., Shillington, D.J., Gaherty, J.B., Scholz, C.A., Nyblade, A.A., Chindandali, P. R.N., Kamihanda, G., McCartney, T., Wood, D., Ferdinand-Wambura, R., 2018. Constraints on rift basin structure and border fault growth in the Northern Malawi Rift from 3-D seismic refraction imaging. J. Geophys. Res. Solid Earth 123, 10003–10025.

Adams, A., Nyblade, A., Weeraratne, D., 2012. Upper mantle shear wave velocity structure beneath the East African Plateau: evidence for a deep, plateauwide low velocity anomaly. Geophys. J. Int. 189, 123–142.

Afonso, J.C., Ben-Mansour, W., O'Reilly, S.Y., Griffin, W.L., Salajegheh, F., Foley, S., Begg, G., Selway, K., Macdonald, A., Januszczak, N., Fomin, I., Nyblade, A., Yang, Y., 2022. Thermochemical structure and evolution of cratonic lithosphere in central and southern Africa. Nat. Geosci. 15, 405–410.

Ajala, R., Persaud, P., 2021. Effect of merging multiscale models on seismic wavefield predictions near the southern San Andreas fault. J. Geophys. Res. Solid Earth 126, 1–23.

Ajala, R., Persaud, P., 2022. Ground-motion evaluation of hybrid seismic velocity models. Seism. Record 2, 186–196.

Ajala, R., Kolawole, F., Legre, J., Olugboji, T., van Herwaarden, D.-P., Fichtner, A., 2026a. Lithospheric structure model compilations and thinning factors from active and passive seismic data in the East African Rift System. Zenodo. 2026. https://doi.org/10.5281/zenodo.20788349 (accessed 22 June 2026).

Ajala, R., Kolawole, F., Legre, J., Olugboji, T., van Herwaarden, D.-P., Fichtner, A., 2026b. Reproducibility material for "Crustal and lithospheric mantle thinning variations beneath the East African Rift System". Zenodo. 2026. https://doi.org/10.5281/zenodo.20788373 (accessed 22 June 2026).

Ajala, R., Kolawole, F., Legre, J., Olugboji, T., van Herwaarden, D.-P., Fichtner, A., 2026c. Lithosphere-asthenosphere boundary map of the African Plate. Zenodo. 2026. https://doi.org/10.5281/zenodo.20788317 (accessed 22 June 2026).

Ajala, R., Kolawole, F., Menke, W., 2024. Blind magmatism abets nonvolcanic rifting. Commun. Earth Environ. 5, 1–8.

Ajala, R., Kolawole, F., Share, P.E., Sahakian, V., Delph, J.R., Hooft, E., He, B., 2025. Toward an accessible framework for synthesizing solid earth models across multiple scales. In: Seismological Society of America Annual Meeting. Baltimore, Maryland, USA, vol. 96, p. 1364.

Aktag, A., Sayit, K., Furman, T., Peters, B.J., 2024. Delamination magmatism in Eastern Anatolia: a geochemical perspective. Geochem. Geophys. Geosyst. 25, 1–18.

Allen, P.R., Allen, J.R., 2005. Basin Analysis Principles and Applications. Blackwell Publishing Company, USA, p. 549.

Baranov, A., Tenzer, R., Ghomsi, F.E.K., 2023. A new Moho map of the African continent from seismic, topographic, and tectonic data. Gondwana Res. 124, 218–245.

Bastow, I.D., Keir, D., Daly, E., 2011. The ethiopian afar geoscientific lithospheric experiment (EAGLE): probing the transition from continental rifting to incipient seafloor spreading. In: Beccaluva, L., Bianchini, G., Wilson, M. (Eds.), Volcanism and Evolution of the African Lithosphere. Geological Society of America Special Paper, Boulder, USA, p. 478.

Birt, C.S., Maguire, P.K.H., Khan, M.A., Thybo, H., Keller, G.R., Patel, J., 1997. The influence of pre-existing structures on the evolution of the southern Kenya Rift Valley – evidence from seismic gravity studies. Tectonophysics 278, 211–242.

Borrego, D., Nyblade, A.A., Accardo, N., Gaherty, J.B., Ebinger, C.J., Shillington, D.J., Chindandali, P., Mbogoni, G., Ferdinand-Wambura, R., Mulibo, G.D., O'Donnell, J. P., Kachingwe, M., Tepp, G., 2018. Crustal structure surrounding the northern

Malawi rift and beneath the Rungwe Volcanic Province, East Africa. Geophys. J. Int. 215, 1410–1426.
Boyce, A., Kounoudis, R., Bastow, I.D., Cottaar, S., Ebinger, C.J., Ogden, C.S., 2023. Mantle wavespeed and discontinuity structure below East Africa: implications for Cenozoic hotspot tectonism and the development of the Turkana Depression. Geochem. Geophys. Geosyst. 24, 1–18.
Braile, L.W., Wang, B., Daudt, C.R., Keller, G.R., Patel, J.P., 1994. Modeling the 2-D seismic velocity structure across the Kenya rift. Tectonophysics 236, 251–269.
Brun, J.P., Beslier, M.O., 1996. Mantle exhumation at passive margins. Earth Planet. Sci. Lett. 142, 161–173.
Brune, S., Heine, C., Perez-Gussinye, M., Sobolev, S.V., 2014. Rift migration explains continental margin asymmetry and crustal hyper-extension. Nat. Commun. 5, 1–9.
Brune, S., Kolawole, F., Olive, J.A., Stamps, D.S., Buck, W.R., Buiter, S.J.H., Furman, T., Shillington, D.J., 2023. Geodynamics of continental rift initiation and evolution. Nature 4, 235–253.
Brune, S., Popov, A.A., Sobolev, S.V., 2012. Modeling suggests that oblique extension facilitates rifting and continental break-up. J. Geophys. Res. Solid Earth 117, 1–16.
Buck, W.R., 2004. Consequences of asthenospheric variability on continental rifting. In: Karner, G.D., Taylor, B., Driscoll, N.W., Kohlstedt, D.L. (Eds.), Rheology and Deformation of the Lithosphere at Continental Margins. Columbia University Press, New York, vol. 1, pp. 1–30.
Buck, W.R., Martinez, F., Steckler, M.S., Cochran, J.R., 1988. Thermal consequences of lithospheric extension: pure and simple. Tectonics 7, 213–234.
Celli, N.L., Lebedev, S., Schaeffer, A.J., Gaina, C., 2020. African cratonic lithosphere carved by mantle plumes. Nat. Commun. 11, 1–10.
Chambers, E.L., Harmon, N., Rychert, C.A., Gallacher, R.J., Keir, D., 2022. Imaging the seismic velocity structure of the crust and upper mantle in the northern East African Rift using Rayleigh wave tomography. Geophys. J. Int. 230, 2036–2055.
Chapman, D.S., 1986. Thermal gradients in the continental crust. Geol. Soc. Spec. Publ. 24, 63–70.
Chenin, P., Manatschal, G., 2025. Fingerprints of necking domains at rifted margins: a review of the best-documented examples worldwide. Earth-Sci. Rev. 265, 105110.
Chenin, P., Manatschal, G., Ghienne, J.F., Chao, P., 2021. The syn-rift tectono-stratigraphic record of rifted margins (Part II): a new model to break through the proximal/distal interpretation frontier. Basin Res. 34, 489–532.
Chenin, P., Schmalholz, S.M., Manatschal, G., Karner, G.D., 2018. Necking of the lithosphere: a reappraisal of basic concepts with thermo-mechanical numerical modeling. J. Geophy Res. Solid Earth 123, 5279–5299.
Chorowicz, J., Collet, B., Bonavia, F.F., Mohr, P., Parrot, J.F., Korme, T., 1998. The Tana basin, Ethiopia: intra-plateau uplift, rifting and subsidence. Tectonophysics 295, 351–367.
Chorowicz, J., 2005. The East African Rift System. J. Afr. Earth Sci. 43, 379–410.
Civiero, C., Goes, S., Hammond, J.O., Fishwick, S., Ahmed, A., Ayele, A., Doubre, C., Goitom, B., Keir, D., Kendall, J.M., Leroy, S., Ogubazghi, G., Rumpker, G., Stuart, S. W., 2016. Small-scale thermal upwellings under the northern East African Rift System from S travel time tomography. J. Geophys. Res. Solid Earth 121, 7395–7408.
Corti, G., 2009. Continental rift evolution: from rift initiation to incipient break-up in the Main Ethiopian Rift, east Africa. Earth Sci. Rev. 96, 1–53.
Corti, G., 2012. Evolution and characteristics of continental rifting: analog modeling-inspired view and comparison with examples from the East African Rift System. Tectonophysics 522, 1–33.
Domingues, A., Silveira, G., Ferreira, A.M.G., Chang, S.J., Custodio, S., Fonseca, J.F., 2016. Ambient noise tomography of the East African Rift in Mozambique. Geophys. J. Int. 204, 1565–1578.
Dugda, M.T., Nyblade, A.A., 2006. New constraints on crustal structure in eastern Afar from the analysis of receiver functions and surface wave dispersion in Djibouti. In: Yirgu, G., Ebinger, C.J., Maguire, P.K.H. (Eds.), The Afar Volcanic Province within the East African Rift System. Geological Society of London, Special Publications, London, pp. 239–251.
Dugda, M.T., Nyblade, A.A., Julia, J., Langston, C.A., Ammon, C.J., Simiyu, S., 2005. Crustal structure in Ethiopia and Kenya from receiver function analysis: implications for rift development in eastern Africa. J. Geophys. Res. 110, 1–15.
Dziewonski, A.M., Anderson, D.L., 1981. Preliminary reference earth model. Phys. Earth Planet. Inter. 25, 297–356.
Ebinger, C.J., 1989. Tectonic development of the western branch of the East African Rift System. Geol. Soc. Am. Bull. 101, 885–903.
Ebinger, C., 2005. Continental break-up: the East African perspective. Astron. Geophys. 46, 2.16–12.21.
Ebinger, C.J., Sleep, N.H., 1998. Cenozoic magmatism throughout east Africa resulting from impact of a single plume. Nature 395, 788–791.
Emry, E.L., Shen, Y., Nyblade, A.A., Flinders, A., Bao, X., 2019. Upper mantle earth structure in Africa from full-wave ambient noise tomography. Geochem. Geophys. Geosyst. 20, 120–147.
Evain, M., Schnurle, P., Lepretre, A., Verrier, F., Watremez, L., Thompson, J.O., de Clarens, P., Aslanian, D., Moulin, M., 2021. Crustal structure of the East African Limpopo margin, a strike-slip rifted corridor along the continental Mozambique Coastal Plain and North Natal Valley. Solid Earth 12, 1865–1897.
Fishwick, S., 2010. Surface wave tomography: imaging of the lithosphere-ashenosphere boundary beneath central and southern Africa? Lithos 120, 63–73.
Fletcher, A.W., Abdelsalam, M.G., Emishaw, L., Atekwana, E.A., Lao-Davilla, D.A., Ismail, A., 2018. Lithospheric controls on the rifting on the Tanzanian Craton at the Eyasi Basin, eastern branch of the East African Rift System. Tectonics 37, 2818–2832.
Fletcher, R.C., Hallet, B., 1983. Unstable extension of the lithosphere: a mechanical model for basin-and-range structure. J. Geophys. Res. 88, 7457–7466.
Fritz, H., Abdelsalam, M., Ali, K.A., Bingen, B., Collins, A.S., Fowler, A.R., Ghebreab, W., Hauzenberger, C.A., Johnson, P.R., Kusky, T.M., Macey, P., Muhongo, S., Stern, R.J., Viola, G., 2013. Orogen styles in the East African Orogen: a review of the Neoprotorozic to Cambrian tectonic evolution. J. Afr. Earth Sci. 86, 65–106.
Fu, H.Y., Li, Z.H., 2024. Roles of continental mid-lithosphere discontinuity in the craton instability under variable tectonic regimes. J. Geophys. Res. Solid Earth 129, 1–27.
Furman, T., 2007. Geochemistry of East African Rift basalts: an overview. J. Afr. Earth Sci. 48, 147–160.
Furman, T., Nelson, W.R., Elkins-Tanton, L.T., 2016. Evolution of the East African Rift: drip magmatism, lithospheric thinning and mafic volcanism. Geochem. Cosmochim. Acta 185, 418–434.
Gajewski, D., Schulte, A., Riaroh, D., Thybo, H., 1994. Deep seismic souding in the Turkana depression, northern Kenya Rift. Tectonophysics 236, 165–178.
Gallacher, R.J., Keir, D., Harmon, H., Stuart, G., Leroy, S., Hammond, J.O., Kendall, J.M., Ayele, A., Goitom, B., Ogubazghi, G., Ahmed, A., 2016. The initiation of segmented buoyancy-driven melting during continental breakup. Nat. Commun. 7, 1–9.
Gao, S.S., Liu, K.H., Reed, C.A., Yu, Y., Massinque, B., Mdala, H., Moidaki, M., Mutamina, D., Atekwana, E.A., Ingate, S., Reusch, A.M., 2013. Seismic arrays to study African rift initiation. Eos Transactions 94, 213–214.
Grant, C., Kolawole, F., Williams, J., 2024. Evolution of rift faulting in incipient, magma-poor divergent plate boundaries: new insights from the Okavango-Makgadikgadi Rift Zone, Botswana. Earth Planet. Sci. Lett. 646, 1–15.
Goes, S., Govers, R., Vacher, A.P., 2000. Shallow mantle temperatures under Europe from P and S wave tomography. J. Geophys. Res. 105, 11153–11169.
Hammond, J.O., Kendall, J.M., Stuart, G.W., Keir, D., Ebinger, C., Ayele, A., Belachew, M., 2011. The nature of the crust beneath the Afar triple junction: evidence from receiver functions. Geochem. Geophys. Geosyst. 12, 1–24.
Hodgson, I., Illsley-Kemp, F., Gallacher, R.J., Keir, D., Ebinger, C.J., Mtelela, K., 2017. Crustal structure at a young continental rift: a receiver function study from the Tanganyika Rift. Tectonics 36, 1–17.
Holtzman, B.K., Kendall, J.M., 2010. Organized melt, seismic anisotropy, and plate boundary lubrication. Geochem. Geophys. Geosyst. 11, 1–29.
Hopper, E., Gaherty, J.B., Shillington, D.J., Accardo, N.J., Nyblade, A.A., Holtzman, B.K., Havlin, C., Scholz, C.A., Chindandali, P.R., Ferdinand, R.W., Mulibo, G.D., Mbogoni, G., 2020. Preferential localized thinning of lithospheric mantle in the melt-poor Malawi Rift. Nat. Geosci. 13, 584–589.
Innocenzi, F., Ezad, I.S., Ronca, S., Agostini, S., Lustrino, M., Foley, S.F., 2024. Experimental petrology constraints on kamafugitic magmas. Eur. J. Mineral. 36, 899–916.
Ji, T., Wen, Z., Wang, Z., Song, C., He, Z., Chen, X., Li, H., Shen, Y., 2023. Structural differences and exploration potential of basins in the eastern and western branches of the East African Rift System. Energy Explor. Exploit. 42, 900–928.
Jones, D.J.R., 2020. A summary of the East African Rift Temperature and Heat Flow Model (EARTH). British Geological Survey Open Report OR/20/006. British Geological Survey, Keyworth, Nottingham, UK, pp. 1–24.
Kachingwe, M., Nyblade, A., Julia, J., 2015. Crustal structure of Precambrian terranes in the southern African subcontinent with implications for secular variation in crustal genesis. Geophys. J. Int. 202, 533–547.
Katumwehe, A.B., Abdelsalam, M.G., Atekwana, E.A., 2015. The role of pre-existing Precambrian structures in rift evolution: the Albertine and Rhino grabens, Uganda. Tectonophysics 646, 117–129.
Kelemen, P.B., Dick, H.J., 1995. Focused melt flow and localized deformation in the upper mantle: Juxstaposition of replacive dunite and ductile shear zones in the Josephine peridotite, SW Oregon. J. Geophys. Res. 100, 423–438.
Khan, M.A., Mechie, J., Birt, C., Byrne, G., Gaciri, S., Jacob, B., Keller, G.R., Maguire, P.K. H., Novak, O., Nyambok, I.O., Patel, J.P., Prodehl, C., Riaroh, D., Simiyu, S., Thybo, H., 1999. The lithospheric structure of the Kenya Rift as revealed by wide-angle seismic measurements. Geol. Soc. Lond. 164, 257–269.
Kibret, B.A., Ayele, A., Keir, D., 2019. Crustal thickness estimates beneath four seismic stations in Ethiopia inferred from p-wave receiver function studies. J. Afr. Earth Sci. 150, 264–271.
Kolawole, F., Ajala, R., 2024. Propagating rifts: the roles of crustal damage and ascending mantle fluids. Solid Earth 15, 747–762.
Kolawole, F., Atekwana, E.A., Lao-Davilla, D.A., Abdelsalam, M.G., Chindandali, P.R., Salima, J., Kalindekafe, L., 2018. Active deformation of Malawi rift's north basin Hinge zone modulated by reactivation of preexisting Precambrian Shear zone fabric. Tectonics 37, 683–704.
Kolawole, F., Firkins, M.C., Al Wahaibi, T.S., Atekwana, E.A., Soreghan, M.J., 2021a. Rift interaction zones and the stages of rift linkage in active segmented continental rift systems. Basin Res. 33, 1–37.
Kolawole, F., Philips, T.B., Atekwana, E.A., Jackson, C.A.L., 2021b. Structural inheritance controls strain distribution during early continental rifting, Rukwa Rift. Front. Earth Sci. 9, 1–14.
Koptev, A., Calais, E., Burov, E., Leroy, S., Gerya, T., 2015. Dual continental rift systems generated by plume-lithosphere interaction. Nat. Geosci. 8, 388–392.
Korostelev, F., Lu, Y., Magrini, F., Boschi, L., Leroy, S., Vetel, W., 2022. Images of the East African Rift System by global adaptive-resolution surface-wave tomography. J. Geophys. Res. Solid Earth 127, 1–18.
Kounoudis, R., Bastow, I.D., Ebinger, C.J., Ogden, C.S., Ayele, A., Bendick, R., Marilta, N., Kianji, G., Wigham, G., Musila, M., Kibret, B., 2021. Body-wave tomographic

imaging of the Turkana depression: implications for rift development and plume-lithosphere interactions. Geochem. Geophys. Geosyst. 22, 1–27.
Kreemer, C., Blewitt, G., Klein, E.C., 2014. A geodetic plate motion and Global Strain Rate Model. Geochem. Geophys. Geosyst. 15, 3849–3889.
Langston, C.A., 1979. Structure under Mount Rainier, Washington, inferred from teleseismic body waves. J. Geophys. Res. 84, 4749–4762.
Last, R.J., Nyblade, A.A., Langston, C.A., 1997. Crustal structure of the East African Plateau from receiver functions and Rayleigh wave phase velocities. J. Geophys. Res. 102, 24469–24483.
Laske, G., Masters, G., Ma, Z., Pasyanos, M., 2013. Update on CRUST1.0 - A 1-degree global model of Earth's crust. In: European Geosciences Union General Assemby 2013. Vienna, Austria, vol. 15, p. 2658.
Lavayssière, A., Drooff, C., Ebinger, C.J., Gallacher, R., Illsley-Kemp, F., Oliva, S.J., Keir, D., 2019. Depth extent and kinematics of faulting in the southern Tanganyika Rift, Africa. Tectonics 38, 842–862.
Lavier, L.L., Manatschal, G., 2006. A mechanism to thin the continental lithosphere at magma-poor margins. Nature 440, 324–328.
Lepretre, A., Schnurle, P., Evain, M., Verrier, F., Moorcroft, D., de Clarens, P., Corela, C., Afilhado, A., Loureiro, A., Leroy, S., d'Acremont, E., Thompson, J., Aslanian, D., Moulin, M., 2021. Deep structure of the North Natal Valley (Mozambique) using combined wide-angle and reflection seismic data. J. Geophys. Res. Solid Earth 126, 1–28.
Legre, J.J., Olugboji, T., 2025. The origins of Africa's upper mantle discontinuities. Geochem. Geophys. Geosyst. 26, 1–15.
Legre, J., Olugboji, T., 2024. East Africa's layering imaged with CRISP-RF. Zenodo. 2026. https://doi.org/10.5281/zenodo.14397996 (accessed 15 April).
Lithgow-Bertelloni, C., Silver, P.G., 1998. Dynamic topography, plate driving forces and the African superswell. Nature 395, 269–271.
Liu, L., Tong, S., Li, S., Qaysi, S., 2020. Sp receiver-function images of African and Arabian lithosphere: survey of newly available broadband data. Seismol. Res. Lett. 91, 1813–1819.
Macgregor, D., 2015. History and the development of the East African Rift System: a series of interpreted maps through time. J. Afr. Earth Sci. 101, 232–252.
Mackenzie, G.D., Thybo, H., Maguire, P.K.H., 2005. Crustal velocity structure across the Main Ethiopian Rift: results from two-dimensional wide-angle seismic modelling. Geophys. J. Int. 162, 994–1006.
Maguire, P.K.H., Keller, G.R., Klemperer, S.L., Mackenzie, G.D., Keranen, K., Harder, S., O'Reilly, B., Thybo, H., Asfaw, L., Khan, M.A., Amha, M., 2006. Crustal structure of the northern Main Ethiopian Rift from the EAGLE controlled-source survey; a snapshot of incipient lithospheric break-up. In: Yirgu, G., Ebinger, C.J., Maguire, P.K.H. (Eds.), The Afar Volcanic Province within the East African Rift System. The Geological Society of London, London, pp. 269–291.
Maguire, P.K.H., Swain, C.J., Masotti, R., Khan, M.A., 1994. A crustal and uppermost mantle cross-sectional model of the Kenya Rift derived from seismic and gravity data. Tectonophysics 236, 217–249.
Makris, J., Ginzburg, A., 1987. The Afar depression: transition between continental rifting and sea-floor spreading. Tectonophysics 141, 199–214.
Mechie, J., Keller, G.R., Prodehl, C., Gaciri, S., Braile, L.W., Mooney, W.D., Gajewski, D., Sandmeier, K.J., 1994. Crustal structure beneath the Kenya Rift from axial profile data. Tectonophysics 236, 179–200.
Mechie, J., Keller, G.R., Prodehl, C., Khan, M.A., Gaciri, S.J., 1997. A model for the structure, composition and evolution of the Kenya rift. Tectonophysics 278, 95–119.
Michon, L., Famin, V., Quidelleur, X., 2022. Evolution of the East African Rift System from trap-scale to plate-scale rifting. Earth-Sci. Rev. 231, 1–18.
Montesi, L.G., 2013. Fabric development as the key for forming ductile shear zones and enabling plate tectonics. J. Struct. Geol. 50, 254–266.
Morley, C.K., 1999. Influence of preexisting fabrics on rift structure. In: Morley, C.K. (Ed.), Geoscience of Rift Systems - Evolution of East Africa, AAPG Studies in Geology, USA, 44, pp. 151–160.
Moulin, M., Aslanian, D., Evain, M., Lepretre, A., Schnurle, P., Verrier, F., Thompson, J., de Clarens, P., Leroy, S., Dias, N., the PAMELA-MOZ35 Team., 2020. Gondwana breakup: Messages from the North Natal Valley. Terra Nova 32, 205–214.
Moulin, M., Lepretre, A., Verrier, F., Schnurle, P., Evain, M., de Clarens, P., Leroy, S., Dias, N., the PAMELA-MOZ35 Team, 2023. From the Lebombo Monocline to the Mozambique Deep Basin, using combined wide-angle and reflection seismic data. Tectonophysics 855, 1–30.
Muirhead, J.D., Wright, L.J., Scholz, C.A., 2019. Rift evolution in regions of low magma input in East Africa. Earth Planet. Sci. Lett. 506, 332–346.
Muirhead, J.D., Fischer, T.P., Oliva, S.J., Laizer, A., van Wijk, J., Currie, C.A., Lee, H., Judd, E.J., Kazimoto, E., Sano, Y., Takahata, N., Tiberi, C., Foley, S.F., Dufek, J., Reiss, M.C., Ebinger, C.J., 2020. Displaced cratonic mantle concentrates deep carbon during continental rifting. Nature 582, 67–72.
Mulaya, E., Gluyas, J., McCaffrey, K., Phillips, T., Ballentine, C., 2025. Seismic stratigraphic framework, dispersal of depocenters, and helium reservoirs in the Rukwa Rift Basin, Tanzania. Tectonophysics 909, 1–13.
Naliboff, J.B., Buiter, S.H., Peron-Pinvidic, G., Osmundsen, P., Tetreault, J., 2017. Complex fault interaction controls continental rifting. Nat. Commun. 8, 1–9.
NCEI, 2022. NCEI global historical hazard database. https://www.ngdc.noaa.gov/hazel/view/hazards/volcano/ (accessed 10 December 2024).
Njinju, E.A., Atekwana, E.A., Stamps, D.S., Abdelsalam, M., Atekwana, E.A., Mickus, K. L., Fishwick, S., Kolawole, F., Rajaonarison, T.A., Nyalugwe, V.N., 2019. Lithospheric structure of the Malawi Rift: implications for magma-poor rifting processes. Tectonics 38, 1–19.
Nyblade, A.A., 2011. The upper-mantle low-velocity anomaly beneath Ethiopia, Kenya, and Tanzania: constraints on the origin of the African superswell in eastern Africa and plate versus plume models of mantle dynamics. Geol. Soc. Am. 478, 37–50.
Nyblade, A.A., Robinson, S.W., 1994. The African superswell. Geophys. Res. Lett. 21, 765–768.
Novak, O., Prodehl, C., Jacob, A.W.B., Okoth, W., 1997. Crustal structure of the southeastern flank of the Kenya rift deduced from wide-angle P-wave data. Tectonophysics 278, 171–186.
O'Donnell, J.P., Adams, A., Nyblade, A.A., Mulibo, G.D., Tugume, F., 2013. The uppermost mantle shear wave velocity structure of eastern Africa from Rayleigh wave tomography: constraints on rift evolution. Geophys. J. Int. 194, 961–978.
Ogden, C.S., Bastow, I.D., Ebinger, C.J., Ayele, A., Kounoudis, R., Musila, M., Bendick, R., Mariita, N., Kianji, G., Rooney, T.O., Sullivan, G., Kibret, B., 2023. The development of multiple phases of superposed rifting in the Turkana Depression, East Africa: evidence from receiver functions. Earth Planet. Sci. Lett. 609, 1–13.
Ogden, C.S., Bastow, I.D., Gilligan, A., Rondenay, S., 2019. A reappraisal of the H-k stacking technique: implications for global crustal structure. Geophys. J. Int. 219, 1491–1513.
Olugboji, T., Xue, S., Legre, J., Tamama, Y., 2024. Africa's crustal architecture inferred from probabilistic and perturbational inversion of ambient noise: ADAMA. Geochem. Geophys. Geosyst. 25, 1–27.
Petruska, J., Eilon, Z., 2022. Distributed extension across the Ethiopian Rift and plateau illuminated by joint inversion of surface waves and scattered body waves. Geochem. Geophys. Geosyst. 23, 1–24.
Pitcavage, E., Furman, T., Nelson, W.R., Graham, D.W., Shirey, S., Kulyanyingi, P.K., Barifaijo, E., 2023. Geochemical constraints on the origin of primitive potassic lavas in the eastern Virunga Volcanic Province. Geochem. Geophys. Geosyst. 24, 1–18.
Plank, T., Forsyth, D.W., 2016. Thermal structure and melting conditions in the mantle beneath the Basin and Range province from seismology and petrology. Geochem. Geophys. Geosyst. 17, 1312–1338.
Priestley, K., Ho, T., Takei, Y., McKenzie, D., 2024. The thermal and anisotropic structure of the top 300 km of the mantle. Earth Planet. Sci. Lett. 626, 1–17.
Priestley, K., McKenzie, D., 2013. The relationship between shear wave velocity, temperature, attenuation and viscosity in the shallow part of the mantle. Earth Planet. Sci. Lett. 381, 78–91.
Priestley, K., McKenzie, D., 2006. The thermal structure of the lithosphere from shear wave velocities. Earth Planet. Sci. Lett. 244, 285–301.
Prodehl, C., Fuchs, K., Mechie, J., 1997a. Seismic-refraction studies of the Afro-Arabian rift system – a brief review. Tectonophysics 278, 1–13.
Prodehl, C., Jacob, A.W.B., Thybo, H., Dindi, E., Stangl, R., 1994. Crustal structure on the northeastern flank of the Kenya rift. Tectonophysics 236, 271–290.
Prodehl, C., Ritter, J.R.R., Mechie, J., Keller, G.R., Khan, M.A., Jacob, B., Fuchs, K., Nyambok, I.O., Obel, J.D., Riaroh, D., 1997b. The KRISP94 lithospheric investigation of southern Kenya – the experiments and their main results. Tectonophysics 278, 121–147.
Reed, C.A., Almadani, S., Gao, S.S., Elsheikh, A.A., Cherie, S., Abdelsalam, M., Thurmond, A.K., Liu, K.H., 2014. Receiver function constraints on crustal seismic velocities and partial melting beneath the Red Sea rift and adjacent regions, Afar Depression. J. Geophys. Res. Solid Earth 119, 2138–2152.
Rosendahl, B.R., 1987. Architecture of continental rifts with special reference to East Africa. Annu. Rev. Earth Planet. Sci. 15, 445–503.
Rooney, T.O., 2020. The Cenozoic magmatism of East Africa: Part V – Magma sources and processes in the East African Rift. Lithos 360–361, 1–33.
Rychert, C.A., Hammond, J.O., Harmon, N., Kendall, J., Keir, D., Ebinger, C., Bastow, I. D., Ayele, A., Belachew, M., Stuart, G., 2012. Volcanism in the Afar Rift sustained by decompression melting with minimal plume influence. Nat. Geosci. 5, 406–409.
Sabattier, A., Nyblade, A., 2025. Moho depth and sediment thickness estimates for the coastal basins of southeastern Tanzania and the Mozambique Coastal Plain. Tectonophysics 906, 1–9.
Sapin, F., Ringenbach, J.C., Clerc, C., 2021. Rifted margins classification and forcing parameters. Sci. Rep. 11, 1–17.
Schnurle, P., Lepretre, A., Evain, M., Verrier, F., de Clarens, P., Thompson, J., Dias, N., Afilhado, A., Loureiro, A., Leroy, S., d'Acremont, E., Aslanian, D., Moulin, M., 2023. Crustal structure and stratigraphy of the South Mozambique margin to South Mozambique ridge from combined wide-angle and relection seismic and drill hole data. Earth Space Sci. 10, 1–28.
Scholz, C.A., Shillington, D.J., Wright, L.J., Accardo, N., Gaherty, J.B., Chindandali, P., 2020. Intrarift fault fabric, segmentation, and basin evolution of the Lake Malawi (Nyasa) Rift, East Africa. Geosphere 16, 1–19.
Shaban, S.N., Kolawole, F., Scholz, C.A., 2023. The deep basin and underlying basement structure of the Tanganyika Rift. Tectonics 42, 1–28.
Schouten, T.L., Gebraad, L., Noe, S., Gulcher, A.J., Thrastarson, S., van Herwaarden, D. P., Fichtner, A., 2024. Full-waveform inversion reveals diverse origins of lower mantle positive wave speed anomalies. Sci. Rep. 14, 1–13.
Shillington, D.J., Gaherty, J.B., Ebinger, C.J., Scholz, C.A., Selway, K., Nyblade, A.A., Bedrosian, P.A., Class, C., Nooner, S.L., Pritchard, M.E., Elliot, J., Chindandali, P.R. N., Mbogoni, G., Ferdinand-Wambura, R., Boniface, N., Manya, S., Kamihanda, G., Saria, E., Mulibo, G.D., Salima, J., Mruma, A., Kalindekafe, L., Accardo, N., Ntambila, D., Kachingwe, M., Mesko, G.T., McCartney, T., Maquay, M., O'Donnell, J.P., Tepp, G., Mtelela, K., Trinhammer, P., Wood, D., Aaron, E., Gibaud, M., Rapa,

M., Pfeifer, C., Mphepo, F., Gondwe, D., Arroyo, G., Eddy, C., Kamoga, B., Moshi, M., . Acquisition of a unique onshore/offshore geophysical and geochemical dataset in the northern Malawi (Nyasa) rift. Seismol. Res. Lett. 87, 1406–1416.
Simon, B., Guillocheau, F., Robin, C., Dauteuil, O., Nalpas, T., Pickford, M., Senut, B., Lays, P., Bourges, P., Bez, M., 2017. Deformation and sedimentary evolution of the Lake Albert rift (Uganda, East African Rift System). Mar. Pet. Geol. 86, 17–37.
Stamps, D.S., Flesch, L.M., Calais, E., 2010. Lithospheric buoyancy forces in Africa from a thin sheet approach. Int. J. Earth Sci. 99, 1525–1533.
Styron, R., Pagani, M., 2020. The GEM global active faults database. Earthq. Spectra 36, 160–180.
Stuart, G.W., Bastow, I.D., Ebinger, C.J., 2006. Crustal structure of the northern Main Ethiopian Rift from receiver function studies. In: Yirgu, G., Ebinger, C.J., Maguire, P.K.H. (Eds.), The Afar Volcanic Province within the East African Rift System. Geological Society, London, Special Publications, London, pp. 253–267.
Sun, M., Gao, S.S., Liu, K.H., Mickus, K., Fu, X., Yu, Y., 2021. Receiver function investigation of crustal structure in the Malawi and Luangwa rift zones and adjacent areas. Gondwana Res. 89, 168–176.
Sutra, E., Manatschal, G., Mohn, G., Unternehr, P., 2013. Quantification and restoration of extensional deformation along the Western Iberia and Newfoundland rifted margins. Geochem. Geophys. Geosyst. 14, 2575–2597.
Tarantola, A., 1984. Inversion of seismic reflection data in the acoustic approximation. Geophysics 49, 1259–1266.
Tesauro, M., Kaban, M.K., Cloetingh, S.A., 2012. Global strength and elastic thickness of the lithosphere. Glob. Planet. Chang. 90–91, 51–57.
Thybo, H., Maguire, P.K.H., Birt, C., Perchuć, E., 2000. Seismic reflectivity and magmatic underplating beneath the Kenya Rift. Geophys. Res. Lett. 27, 2745–2748.
Tiberi, C., Gautier, S., Ebinger, C., Roecker, S., Plasman, M., Albaric, J., Deverchere, J., Peyrat, S., Perrot, J., Wambura-Ferdinand, R., Msabi, M., Muzuka, A., Mulibo, G., Kianji, G., 2019. Lithospheric modification by extension and magmatism at the craton-orogenic boundary: North Tanzania Divergence, East Africa. Geophys. J. Int. 216, 1693–1710.
Tromp, J., 2020. Seismic wavefield imaging of Earth's interior across scales. Nat. Rev. Earth Environ. 1, 40–53.
Twinomujuni, L., Liu, K., Ahmed, K.S., Njabire, N., Sserubiri, T., Namara, B., 2025. Tectonostratigraphic evolution and petroleum potential of the Lake Edward Basin, Uganda: insights from integrated surface and subsurface data analysis. J. Pet. Geol. 49, 193–214.
van Herwaarden, D.P., Thrastarson, S., Halpa, V., Afanasiev, M., Trampert, J., Fichtner, A., 2023. Full-waveform tomography of the African plate using dynamic mini-batches. J. Geophys. Res. Solid Earth 126, 1–22.
Virieux, J., Operto, S., 2009. An overview of full-waveform inversion in exploration geophysics. Geophysics 74, 1–26.
Wang, T., Gao, S.S., Yang, Q., Liu, K.H., 2021. Crustal structure beneath the Ethiopian Plateau and adjacent areas from receiver functions: implications for partial melting and magmatic underplating. Tectonophysics 809, 1–12.
Watremez, L., Leroy, S., d'Acremont, E., Roche, V., Evain, M., Lepretre, A., Verrier, F., Aslanian, D., Dias, N., Afilhado, A., Schnurle, P., Castilla, R., Despinois, F., Moulin, M., 2021. The limpopo magma-rich transform margin, South Mozambique: 1. insights from deep-structure seismic imaging. Tectonics 40, 1–29.
Wessel, P., Luis, J.F., Uieda, L., Scharroo, R., Wobbe, F., Smith, W.H.F., Tian, D., 2019. The generic mapping tools version 6. Geochem. Geophys. Geosyst. 20, 1–20.
Wilson, J.T., 1966. Did the Atlantic close and then re-open? Nature 211, 676–681.
Wolbern, I., Rumpker, G., Schumann, A., Muwanga, A., 2010. Crustal thinning beneath the Rwenzori region, Albertine rift, Uganda, from receiver-function analysis. Int. J. Earth Sci. 99, 1545–1557.
Wright, L.J., Muirhead, J.D., Scholz, C.A., 2020. Spatiotemporal variations in upper crustal extension across the different basement terranes of the Lake Tanganyika Rift, East Africa. Tectonics 39, 1–24.
Zhu, L., Kanamori, H., 2000. Moho depth variation in southern California from teleseismic receiver functions. J. Geophys. Res. Solid Earth 105, 2969–2980.